Applied Geochemistry 187 (2025) 106399

Contents lists available at ScienceDirect

Applied Geochemistry

journal homepage: www.elsevier.com/locate/apgeochem

Mössbauer spectroscopy: a key tool to quantify Fe-speciation and distribution in H_2-generating rocks

U. Geymond [a,b,*], K. Loiseau [c,d], V. Roche [e], G. Pasquet [c], S. Revillon [f], M. Sougrati [g,h], I. Moretti [c]

[a] IPGP, Université Paris-Cité, CNRS-UMR7154, Paris, France
[b] IFP énergies nouvelles, Rueil-Malmaison, France
[c] Laboratoire des Fluides Complexes et leurs Réservoirs, Université de Pau et des Pays de l'Adour, CNRS-UMR5150, Pau, France
[d] CVA Engineering, 2 Rue Johannes Kepler, 64000, Pau, France
[e] Laboratoire de Planétologie et Géosciences, Le Mans Université, CNRS-UMR 6112, Le Mans, France
[f] SEDISOR/GEO OCEAN Univ, Brest-CNRS-IFREMER UMR6538, Plouzané, France
[g] ICGM, Univ. Montpellier, CNRS, ENSCM, 34090, Montpellier, France
[h] UAR Chimie Balard, Univ. Montpellier, CNRS, ENSCM, 34090, Montpellier, France

ARTICLE INFO

Editorial handling by: Wenfeng Tan

Keywords:
Mössbauer spectroscopy
Iron speciation
Natural H_2
Banded iron formations
Iron-rich granite
Peridotite

ABSTRACT

Oxidation of Fe^{2+} by anoxic water in the subsurface is a key geochemical process, contributing to the formation of natural dihydrogen (H_2). The development and application of effective tools to accurately characterize the content and speciation of iron in samples is thus a major concern for H_2 prospection. Traditionally, the study of iron has been conducted through either time-consuming analyses at the micrometer scale or faster analyses at the bulk rock scale, raising concerns about the accuracy and representativeness of the characterization depending on the chosen approach. Moreover, most techniques are typically limited to determining either Fe distribution or Fe speciation, thus necessitating a full series of analyses to reach a comprehensive understanding of the sample. This approach does not align with the need for rapid and numerous characterizations required in H_2 prospection programs. In this study, we investigated the relevance of using Mössbauer Spectroscopy (MS) on complex mineral assemblage, by characterizing five Fe-rich natural samples. Among others, we conclude, based on the quality of the resulting spectra fitting that room-temperature (295K) data collection is more effective than low-temperature (6K) data collection, due to the challenges in deconvoluting the complex spectra of mixed mineral assemblages at low temperature. $Fe^{2+}/\Sigma Fe$ ratios obtained from MS are compared with those derived from conventional Fe^{2+} titration on the same samples. The comparison shows a great correlation between MS and titration results with an average deviation of 0.04 on the $Fe^{2+}/\Sigma Fe$ ratio. This confirms the reliability of MS, providing at the same time insights into both Fe distribution (i.e., Fe mineralogy) and Fe speciation, contrary to titration that only gives access to bulk $Fe^{2+}/\Sigma Fe$ ratio. Finally, results show that the accuracy of MS spectra fitting is significantly influenced by prior knowledge of the sample mineralogy, which can be easily leveraged by rapid and routinely performed characterization techniques (e.g., multispectral mineral imaging).

1. Introduction

Quantifying Fe content, distribution, and speciation in rocks involved in natural dihydrogen (H_2) generation is crucial for accurately assessing H_2 yields resulting from Fe oxidation during fluid-rock interactions. It is thus largely performed during petrographic inspections and experiments (e.g., Malvoisin et al., 2012; McCollom et al., 2016) that will then define places of interest for natural H_2 exploration or stimulated H_2 generation worldwide (Lévy et al., 2023; Osselin et al., 2022; Templeton et al., 2024). Various techniques are commonly employed to access this information. At the bulk rock scale (i.e., in three dimensions), X-ray diffraction (XRD) is commonly utilized to determine mineralogy, providing first-order estimates of iron-bearing minerals' nature and abundances by Rietveld methods (e.g., Carlin et al., 2024). Elementary analyses, by Inductively Coupled Plasma techniques (ICP) coupled with titration, offer more precise iron quantifications, albeit

---

* Corresponding author. IPGP, Université Paris-Cité, CNRS-UMR7154, Paris, France.
E-mail address: geymond@ipgp.fr (U. Geymond).

https://doi.org/10.1016/j.apgeochem.2025.106399
Received 17 December 2024; Received in revised form 14 April 2025; Accepted 14 April 2025

without revealing mineralogical details (e.g., Roche et al., 2024). At the microscale (i.e., in two dimensions), *in-situ* techniques such as Electron Probe Microanalysis (EPMA) or Scanning Transmission X-ray Microscopy (STXM) enable accurate quantification of iron content and speciation within individual minerals (e.g., Combaudon et al., 2024; Pasquet et al., 2021), though requiring considerable time investment due to specific sample preparation and mineral scouting required for analysis. Recently, Kularatne et al. (2024) proposed a novel approach coupling 2D chemical and mineralogical data (EDS-SEM) and 3D imagery (X-ray micro-computed tomography) to quantitatively assess the distribution and speciation of iron at the bulk rock scale, unlocking new perspectives to calculate H_2 generation yields representative of the studied bulk rock sample. However, the success of such a methodology is currently constrained by (i) a high-level pre-knowledge of the sample such as the formula unit of each type of mineral constituting the sample, and (ii) the long time required for data acquisition and subsequent computer processing (e.g., several days considering the whole analytical chain). Furthermore, the literature emphasizes the significant variability in both Fe content and speciation, commonly observed across all scales (ranging from micrometer to outcrop) in samples sharing the same geological age and history (e.g., Andreani et al., 2013b; Loiseau et al., 2024). Therefore, conducting numerous rapid and cost-effective measurements seems essential to prevent erroneous conclusions when assessing rocks' past and remnant H_2-generation potential.

In parallel, Mössbauer Spectroscopy (MS) allows the determination of speciation and distribution of Mössbauer-sensitive elements, such as iron, among the different crystallographic sites of the minerals constitutive of a powder. The theoretical limit of detection reaches down to 1 atomic percent (i.e., 1 % of the ΣFe present in the sample), although the actual sensitivity may be slightly lower due to practical constraints (e.g. signal noise, sample heterogeneity). The principle of MS has been discussed in a wide range of literature reviews (Dyar et al., 2006; Grandjean and Long, 2021; Murad, 2010; Stevens et al., 2005; Yoshida and Langouche, 2013), and an overview of this technique is also provided in Appendix A1 to support the comprehensibility of this study for non--Mössbauer specialists. For decades, this technique has been extensively used in various fields of fundamental research, e.g., mineralogy and crystallography of iron oxides (e.g., Daniels and Rosencwaig, 1969; Gorski et al., 2012; Joos et al., 2016), or more recently in applied research as in the field of new lithium-based batteries (e.g., Fehse et al., 2019; Yamada et al., 2001). In the framework of prospection for natural H_2-generating rocks, the use of MS has remained very sporadic so far, except in a few sparse studies mainly focusing on serpentinization and limited most of the time to the characterization of separate minerals (Geymond et al., 2023; Seyfried et al., 2007; Syverson et al., 2017; Tutolo et al., 2020). Working on a single mineral enhances precision (McGuire et al., 1991), but implies that analyses on bulk natural rocks are precluded by mineral extraction from the rock sample matrix. Such an approach is therefore time-consuming and does not provide information regarding the $Fe^{2+}/\Sigma Fe$ ratio at the bulk scale. If MS analysis of bulk rock samples proves successful in providing accurate $Fe^{2+}/\Sigma Fe$ ratios, this technique could become a gateway for determining H_2 yields of generation, and may therefore play a prominent role in this field of research in the coming years. As with any other analytical tool, however, MS should be used carefully, with consideration of its limitations.

Based on a compilation of petrographic analyses performed on Fe-rich natural samples, this study investigates the possibility of performing MS analyses at the bulk rock scale to get accurate $Fe^{2+}/\Sigma Fe$ ratio quantifications and the respective contribution of each mineral phase, in reasonable time scales. Raw MS data are processed following XRD and Scanning electron microscopy (SEM) analyses, and the results are compared with the $Fe^{2+}/\Sigma Fe$ ratio from titrations performed on the same samples. This study explores the most suitable parameters, (e.g., temperature of spectra acquisition), and approach for framing Fe distribution and speciation in rocks. It also proposes an efficient methodology for natural H_2 exploration purposes.

2. Material and methods

2.1. Analytical strategy

In this paper, MS is used to quantify iron distribution and speciation in Fe-rich rocks with complex paragenesis. Five samples (S1 – S5) were chosen for this study, described in section 2.3. They were selected because (i) they encompass a diverse range of iron content and mineral assemblage typically found in continental regions, in Australia, Namibia and France (Fig. 1), and (ii) all of them are currently being investigated to assess their potential for H_2 generation. Since Fe content significantly impacts the time required to acquire high-quality MS spectra, the first step of this study was to investigate the ΣFe concentrations of the samples by performing bulk elemental analyses using ICP-OES. The ΣFe concentrations in the samples range from 6.82 wt% to 52.90 wt% Fe_2O_3, ensuring that the MS analyses could be conducted under optimal conditions and minimizing analysis time. Details on the ICP-OES methodology and results are provided in Appendices A2 and A3, respectively. As the MS data processing also requires an *a priori* knowledge of bulk Fe-bearing mineralogy, the second step of this study aimed to determine the samples' paragenesis, using conventional analytic methods such as SEM and XRD. Details on these methods are given in Appendix A2. MS data acquisitions were then performed under various setups to investigate the best compromise between precision and time efficiency. Initially, all samples were analyzed at room temperature (295K) and over a wide range of source velocities (i.e., large band) to ensure the detection of species with a broad spectral dispersion. Since the MS spectral signature of magnetic materials is temperature-dependent, a series of high-velocity analyses was also conducted at low temperature (6K), tentatively to achieve more precise quantifications of Fe speciation and distribution, as is commonly done in the literature (e.g., Doriguetto et al., 2003). Analyses were finally conducted over a reduced range of source velocities (i.e., short band) to assess the relevance of this time-saving analysis setup. Practical details regarding MS acquisition and processing are provided in the following subsection. Our $Fe^{2+}/\Sigma Fe$ ratio quantification results obtained by MS were then challenged through a comparison with wet chemistry (Fe^{2+} titration) to ensure the precision of our MS methodology. Details on the titration protocol and raw results are given in Appendices A2 and A3, respectively.

2.2. Mössbauer spectroscopy: data acquisition and processing

^{57}Fe Mössbauer spectra were acquired in transmission mode using a constant acceleration spectrometer with a $^{57}Co/Rh$ source. Measurements were initially conducted at room temperature in a zero-magnetic field. Samples were then cooled in using a vibration-decoupled and closed-cycle helium cryostat, until the low temperature target was reached. The spectra were subsequently collected. The measurements were performed in high velocity (source velocities ranging from −12 to 12 mm/s) and low velocity (from −4 to 4 mm/s). All isomer shifts mentioned are referenced to α-Fe. The fitting of hyperfine parameters was done using a Liouville operator-based program coded in C++, allowing to fit the spectra with appropriate combinations of Lorentzian lines. In this way, the respective subspectral parameters (e.g., the isomer shift) and the relative areas of the different Fe contributions were determined (Sougrati et al., 2008, 2016). The pre-Mössbauer analyses were used as a starting basis for the spectra fitting, in addition to theoretical hyperfine parameters of the minerals, available in the literature and gathered in Appendix A4. Spectra were refined to improve the χ^2 values (ideal fitting $\chi^2 = 1$). However, it is important to remember that the χ^2 value depends not only on the quality of the fit but also on other criteria such as the initial signal-to-noise ratio of the acquired spectra and the number of Fe-contributions fitted. Therefore, even with a reasonably low or high χ^2 value (yet remaining close to $\chi^2 = 1$), a careful visual inspection of the spectral fitting should always prevail to assess the quality of the MS spectrum processing. In this study, MS

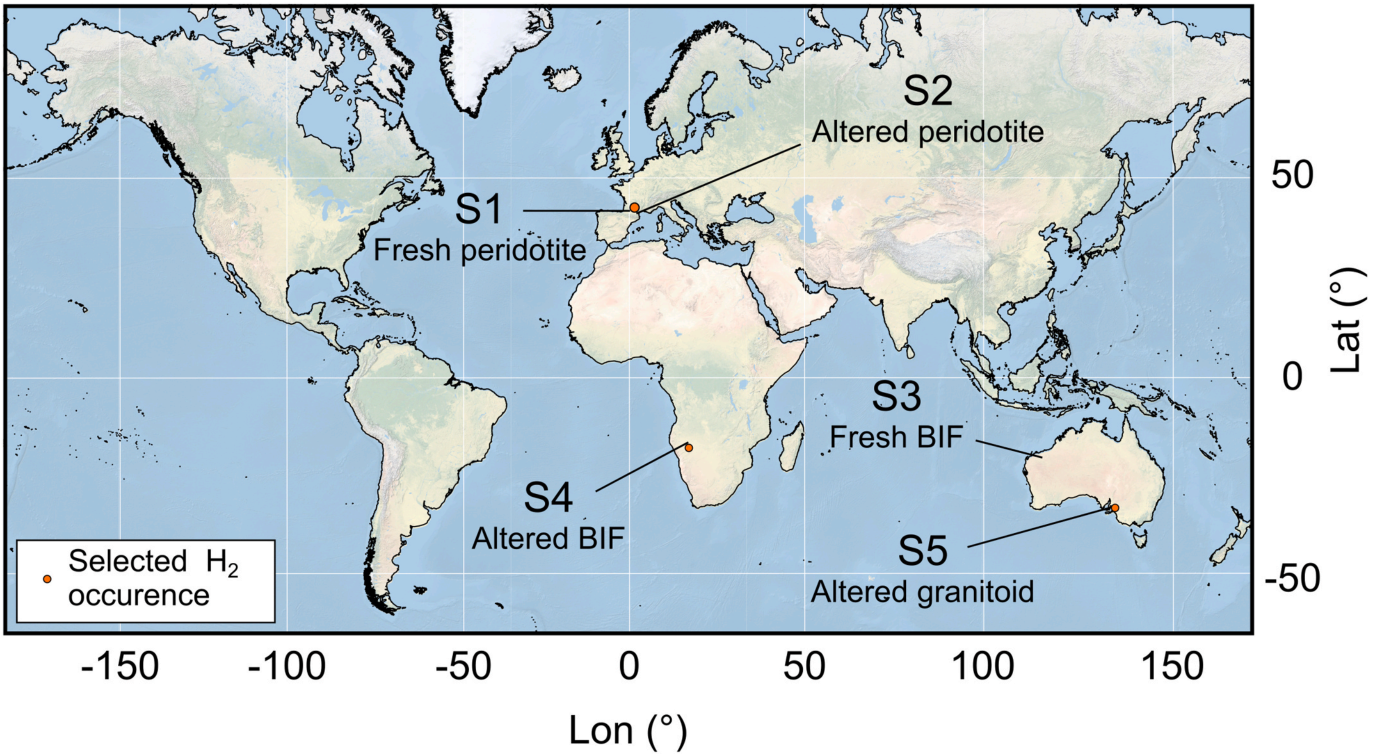

Fig. 1. Sampling locations of the 5 studied samples. S1: Slightly serpentinized Lherzolite from French Pyrenean foothills (1.3716E/42.8045N). S2: Highly serpentinized Lherzolite from French Pyrenean foothills (0.6443W/43.0557N). S3: Fresh Archean BIF from Western Australia (119.0578E 21.2645S). S4: Altered Neoproterozoic BIF from Namibia (16.0307E/28.0307S). S5: Altered Mesoproterozoic Granitoid from Southern Australia (137.76E/34.09S). Four of them are currently under investigation to evaluate their link with natural H_2 seepages occurring in their vicinity.

quantifications are simply derived from the respective subspectrum areas obtained during the spectra fitting. Since there is no consensus on the efficiency of correcting the relative areas of each iron contribution based on their recoilless factor (Dyar, 2002), which is characteristic of each Fe site in a given mineral environment, such a correction was not applied. This approach, which may introduce some bias, is addressed in the discussion (Section 4.3).

2.3. Studied samples

S1 and S2 samples consist of ultrabasic rocks. They represent low-grade and high-grade serpentinized types of the main lithology studied for H_2 generation, particularly in ophiolites (Barnes et al., 1978; Neal and Stanger, 1983). The two samples are lherzolites collected in the Pyrenees Mountains, where natural H_2 seeps have been detected and the exploration is currently active (Lefeuvre et al., 2021; Loiseau et al., 2024). S1 comes from the Etang de Lherz massif in the eastern part of the Pyrenees and is dated between 110 and 85 Ma (Lagabrielle and Bodinier, 2008). It is considered as a sedimentary-type peridotite associated with breccias suggesting an emplacement during the dismantling of the platform (Clerc et al., 2012; Lagabrielle et al., 2010). Its serpentinization grade is less than 10 %, making it one of the least serpentinized rocks in the Pyrenees (Le Roux et al., 2007). S2 comes from the Saraillé Massif, located in the western part of the Pyrenees (Fig. 1). It is a highly-serpentinized tectonic-type peridotite, resulting from the emplacement of the Sarrance anticline (Corre et al., 2016; Lagabrielle et al., 2019).

S3 and S4 are Precambrian-aged Banded Iron Formations (BIF) that have recently been suggested to generate H_2 (Geymond et al., 2022; Moretti et al., 2022; Roche et al., 2024). S3 is a drill core sample from the Archean iron member of the Pincunah Hill Formation (Van Kranendonk, 2006), obtained from 50 to 100 m depth during the drilling of the Iron Bridge Magnetite Project, in the Pilbara Craton (Western Australia, Fig. 1). The iron member age has been constrained isotopically to 3.19 Ga (Rasmussen et al., 2007), and is interlayered with greenstone belts for a total thickness of up to 800 m. S4 is a BIF sample coming from the Neoproterozoic Jakkalsberg Member Unit (Frimmel, 2011) that outcrops near the border between Namibia and South Africa (Fig. 1). It differs significantly from S3 in both age and the degree of metamorphism undergone. No radiometric data is available but micropaleontological data indicates an Ediacaran-aged sediment deposition, around 635 - 541 Ma (Frimmel, 2011). This rock records greenschist-facies metamorphism marking the subsequent collision (Frimmel, 1998).

S5 corresponds to a Fe-rich granite. In addition to the commonly accepted radiolysis (Sherwood Lollar et al., 2014), recent studies suggest that granite may generate H_2 during the weathering of iron-bearing minerals such as biotite or amphibole (Murray et al., 2020; Truche et al., 2021). S5 was collected from a drill core recovered at 86.4 m depth, extracted during the DDH221 drilling campaign performed in Yorke Peninsula (Southern Australia, Fig. 1). It belongs to the intrusive Hiltaba Suite, dated at 1.6 Ga (Reid et al., 2021). This Suite is assumed to play a role in H_2 fluxes measured in Yorke Peninsula (Boreham et al., 2021).

3. Pre-Mössbauer analyses: accurate paragenesis determination

This section aims to describe the specific paragenesis of the samples, with a special focus on Fe-bearing phases. They were determined through optical microscopy, XRD, and SEM. All the Fe minerals, specific to each sample, were then used to efficiently process the raw Mössbauer spectra. Results are presented in the main manuscript for S1 (Fig. 2), and in Appendices A5-A8 for the four other samples. Table 1 summarizes the paragenesis of all the samples.

S1 (slightly serpentinized peridotite) mainly consists of olivine (ideal formula: $[Fe^{2+},Mg]_2SiO_4$), clino- and orthopyroxene (ideal formula:

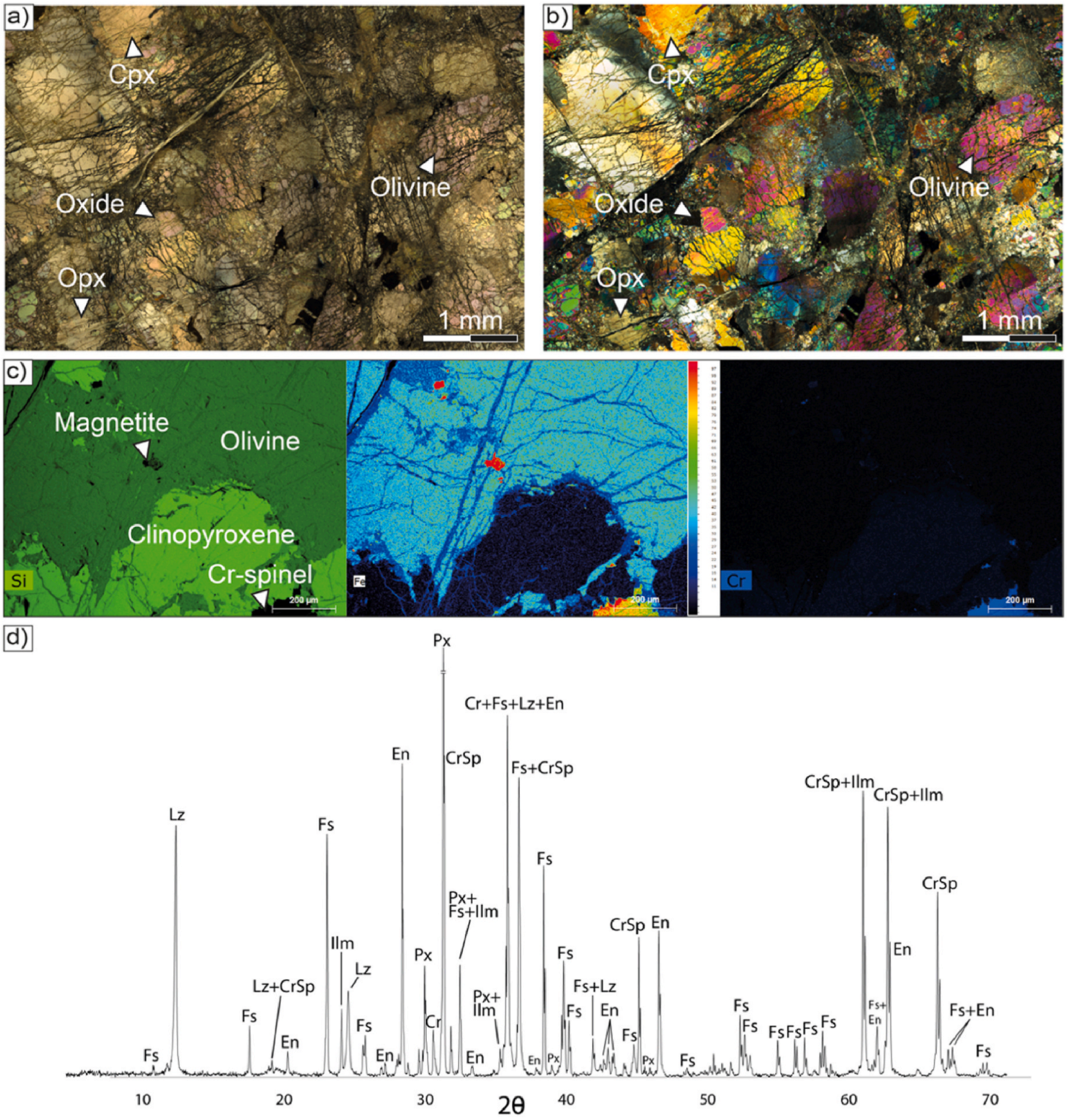

Fig. 2. Initial characterization of the S1 sample. The corresponding results for S2–S5 are provided in Appendices A5-A8. (a,b) Photomicrograph of the thin section observed in Polar-plane light. (c) Elementary mapping highlighting the distribution of Si, Fe, and Cr in the sample. (d) XRD pattern and peak indexing of the bulk sample powder. Fs refers to forsterite, Lz to lizardite, CrSp to Cr-spinel, Ilm to ilmenite, Px to pyroxene. In this sample, Fe is carried by olivine, pyroxene, serpentine, Cr-spinel, and to some extent magnetite and ilmenite.

$[Fe^{2+},Mg,Ca]_2Si_2O_6$), all of which being milli-to plurimillimetric in size. These primary minerals are densely fractured and slightly serpentinized (ideal formula: $[Fe^{2+},Mg]_3Si_2O_5[OH]_4$), as highlighted by both SEM elementary mapping and XRD (Fig. 2). Opaque minerals/oxides are disseminated and are part of the primary paragenesis. Most of them correspond to ilmenite (ideal formula: $Fe^{2+}TiO_3$) and Cr-rich spinel (ideal formula: $Mg[Cr,Al]_2O_4$) according to XRD peak indexing (Fig. 2b), where a significant part of aluminum is substituted by chromium (Fig. 2e). Fe also enters the composition of these oxides (Fig. 2d), substituting either Mg^{2+} as Fe^{2+} or Al^{3+} as Fe^{3+}. By order of decreasing abundances, the main minerals carrying iron in this sample are olivine, pyroxene, serpentine, and spinels. These phases have been used as a starting point to process S1 Mössbauer data. Below XRD detection limit, very sparse magnetite crystals (ideal formula: $Fe^{2+}Fe^{3+}_2O_4$) are also observed in SEM, as well as a few pyrite (ideal formula: $Fe^{2+}S_2$) sporadically found in the rock (Fig. 2c,d).

S2 (highly serpentinized peridotite) is dominated by Fe-poor serpentine (see Appendix A5). A few primary mineral relics of olivine and pyroxene are preserved within serpentine and as mesh texture cores. A notable feature is the presence of 3–6 mm bastite that corresponds to fully pseudomorphosed serpentinized orthopyroxene relicts. The presence of serpentine veins of 0.4 mm might reflect different serpentinization events. Oxides/opaque minerals are widely developed in the mesh texture (~10 vol% of the paragenesis) and correspond to primary Cr-rich spinel (~1 mm) and aggregates of smaller magnetite occurring at chromite edges.

S3 (Archean BIF) paragenesis is consistent with the descriptions of the Iron Member of the Pincunah Hill Formation (Trendall and Blockey, 1970), corresponding to thinly layered cherty levels (ideal formula: SiO_2) and Fe-oxide levels (see Appendix A6). Oxides/opaque minerals are essentially magnetite. In addition to these dominant constituents, our analyses reveal the presence of accessory minerals such as albite

Table 1

Summary of the Fe-bearing minerals constituting the studied samples. Ol refers to olivine, Cpx to clinopyroxene, Opx to orthopyroxene, Serp to serpentine, CrSp to Cr-spinel, Mgt to magnetite, Carb to Fe-carbonate, Bi to biotite, Chl to chlorite, Py to pyrite, Stilp to stilpnomelane, Hem to hematite and Ilm to ilmenite. Due to the minor amounts observed in the sample for Py, Stilp and Ilm, these phases are not expected to contribute to the MS spectra but were tentatively fitted. « + » symbol describes the relative volume abundances. Both Fe^{2+} and Fe^{3+} are commonly found in most of these minerals, demonstrating the relevance of performing MS analyses.

Sample	Observed Fe-bearing minerals in the paragenesis									
	Ol	Cpx	Opx	Serp	CrSp	Mgt	Carb	Bi	Chl	minor
S1	+++	+++	+++	+	+++	+				Py, Ilm
S2	+	+	+	+++	+	+++				
S3						+++	+++			Stilp, Hem
S4						+++		+++	+	
S5						+++		+++	+	Ilm

(ideal formula: $NaAlSi_3O_8$). Some of them contain significant iron contents such as Fe-bearing dolomite (ideal formula: $[Fe^{2+},Ca,Mg]_2[CO3]_2$) and stilpnomelane (ideal formula: $K[Fe^{2+},Mg,Fe^{3+}]_8[Si,Al]_{12}[O,OH]_{27}.nH_2O$).

S4 (Neoproterozoic BIF) is predominantly made up of quartz and fine-grained magnetite (c. 5–10 μm) disseminated in the bulk rock (see Appendix A7). Fe-bearing biotite is also observed (ideal formula: $K[Fe^{2+},Mg,Fe^{3+}]_3[Si,Fe^{3+},Al]_4O_{10}[OH]_2$). Minor components complete the paragenesis such as Fe-bearing chlorite (ideal formula: $[Fe^{2+},Mg,Fe^{3+}]_6[Si,Al]_4O_{10}[OH]_8$).

S5 (Hiltaba granite) consists mostly of quartz, albite, K-feldspar (ideal formula: $KAlSi_3O_8$), and biotite (see Appendix A8). The latter appears altered into chlorite and both minerals contain iron although the Fe content is higher in biotite. Disseminated minerals of primary origin occur locally and correspond to apatite (ideal formula: $Ca_5[PO_4]_3[OH,F,Cl]$), magnetite, and ilmenite.

4. Mössbauer results and discussion

The following section presents the MS processing results for both low-temperature (6K) and room-temperature (295K) acquisitions in high-velocity and low-velocity. All raw data can be found in supplementary material. The hyperfine parameters used to perform the processing were selected from an abacus of hyperfine parameters of each mineral of interest for H_2 generation, built for the specific purpose of this study and available in Appendix A4. The details of each spectrum fitting discussed in this section are provided in Appendix A9.

4.1. *High-velocity spectra*

4.1.1. *Qualitative room-temperature fitting*

Except for S1 (Fig. 3a), all samples exhibit sextets at 295K, indicating the presence of at least one Fe-bearing magnetic phase (Fig. 3b–e) and justifying the acquisition of high-velocity spectra. The processing was initiated by fitting the sextets to help later constrain the respective contributions of doublets in the inner part of the spectrum. Using the initial sample characterization results, two sextets were successfully fitted for the S2–S5 acquisitions with the hyperfine parameters of magnetite (see abacus in Appendix A4). These two sextets represent Fe distributed in the tetrahedral site $()_A$ as Fe^{3+} and in the octahedral site $[]_B$ as both Fe^{2+} and Fe^{3+}, with respect to the ideal magnetite structural formula $(Fe_8^{3+})_A[Fe_8^{3+},Fe_8^{2+}]_BO_{32}$. Electron hopping between Fe^{2+} and Fe^{3+} in sites $[]_B$ above the Vervey transition ($T_V \sim 120K$) results in a mean ionic charge of $Fe^{2.5+}$. The apparent quality of the sextets fitting indicates that, within the detection limit, no other Fe-bearing magnetic phases are present in the S2–S5 samples.

At 295K, the S1 spectrum (Fig. 3a) was fitted with two contributions of olivine, corresponding to the M1 and M2 octahedral sites where Fe^{2+} can occur. It must be noted that hyperfine parameters of Fe^{2+} in the M2 site of olivine are hardly distinguishable from Fe^{2+} in serpentine (see specific hyperfine parameters of each mineral in Appendix A4). However, the low amount of serpentine present in S1 as well as iron poorness in serpentine versus olivine highly suggest that this contribution is related to olivine. It highlights the need to have an *a priori* knowledge of the sample before MS processing. Two contributions were successfully attributed to pyroxene although three crystallographic sites can theoretically incorporate Fe in such a mineral. This can be explained by the iron poorness of pyroxene in this rock. One final contribution was fitted, corresponding to Fe^{3+} in Cr-rich spinel. Since a few sparse magnetite growths were observed in S1 under SEM, it may seem puzzling that no contribution from magnetite was fitted. However, it only reflects the amounts of Fe present in olivine and pyroxene, which "overprint" the small contribution of Fe from magnetite (theoretical detection limit of 1 % atomic $\sum$Fe, though slightly higher in practice). For S2 (Fig. 3b), only one contribution of Fe^{2+} was evidenced in serpentine, although serpentine is thought to incorporate one octahedral Fe^{2+}, one octahedral Fe^{3+}, and one tetrahedral Fe^{3+} (Fuchs et al., 1998; Tutolo et al., 2020). Fe^{3+} in Cr-rich spinel was also revealed and no Fe^{2+} could be fitted for this phase. For S3 (Fig. 3c), one doublet was fitted corresponding to a Fe^{2+} contribution from Fe-carbonate. Since carbonate only incorporates Fe^{2+} in one single crystallographic site with similar hyperfine parameters regardless of the exact nature of the carbonate (e.g., ankerite or siderite), the nature of the carbonate cannot be determined unambiguously. For S4 (Fig. 3d), two contributions were fitted from biotite, corresponding to one Fe^{2+} and one Fe^{3+}, both of them in octahedral position. A contribution of chlorite was tentatively added during the processing without success, suggesting a very minor contribution from chlorite in the total Fe budget, which is consistent with the low amount of chlorite in the sample according to XRD. For S5 (Fig. 3e), three distinct contributions were identified from biotite, corresponding to two Fe^{2+} and one Fe^{3+}, all of them in octahedral position. This demonstrates that a high level of precision can be achieved to characterize one single mineral in a complex mineral assemblage. Despite prior analyses highlighting the presence of chlorite and titanite as additional Fe-bearing phases, no contribution from them could successfully be fitted to the spectrum.

4.1.2. *Qualitative low-temperature fitting*

A common reason for conducting low-temperature MS analyses is to detect the presence of magnetic phases, that typically exhibit sextets below their temperature of ordering, while they present only doublet at 295K. For our samples analyzed at 6K, S1 still exhibits only doublets as

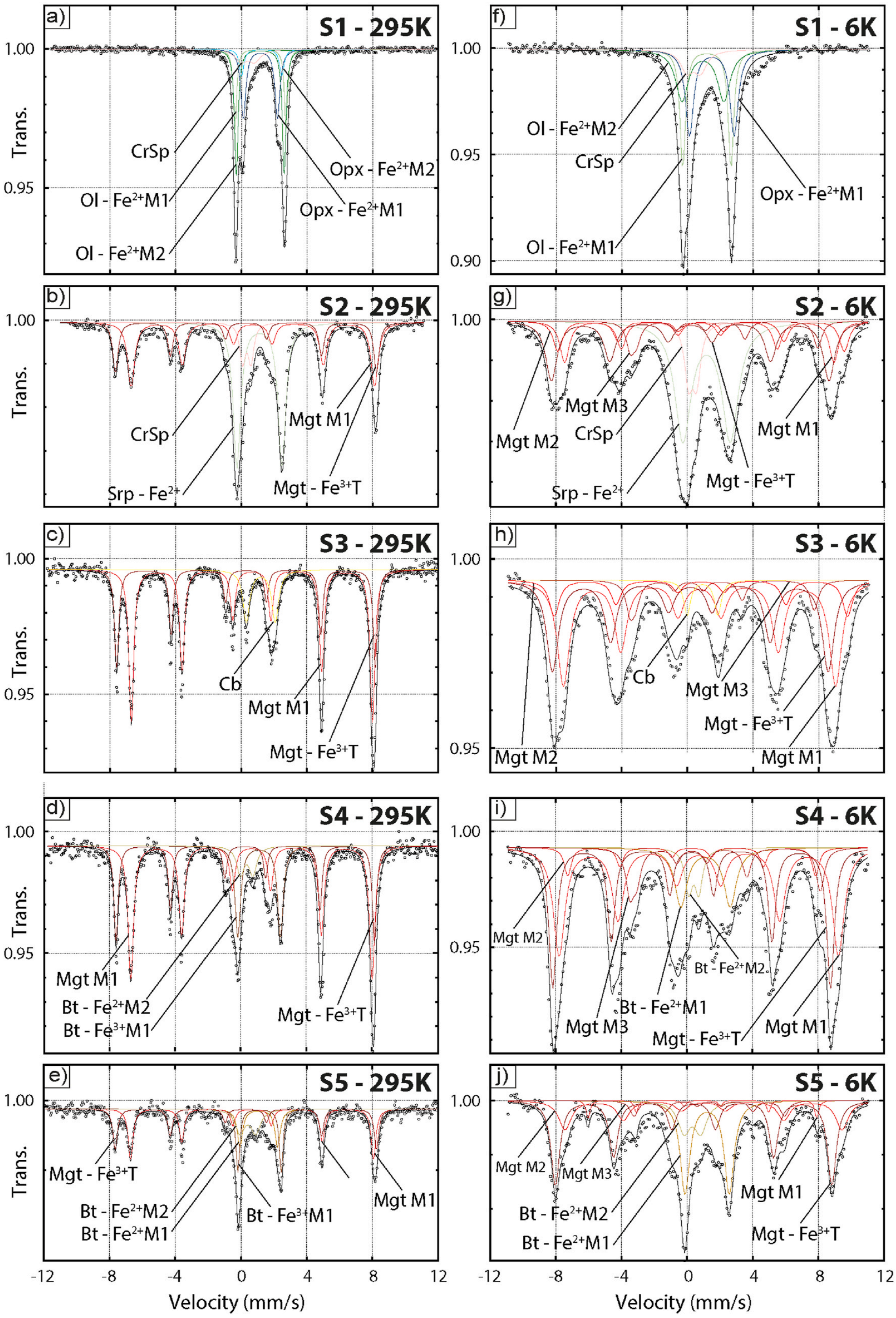

Fig. 3. MS spectra fitting for data collected in high-velocity at (a–e) 295K and (f–j) 6K. The χ^2 are provided for each fit in Appendix A9. Fe occupies either octahedral sites (M) and/or tetrahedral sites (T) in silicate and oxides. Dots correspond to the raw data and the black line to the fitting result. Abbreviations remain identical as the one provided previously. For more quantitative information regarding the relative areas of each subspectrum, see section 4.3.

for the acquisition at 295K (Fig. 3f). The absence of any sextet even at such a low temperature provides robust evidence that only trace amounts of magnetic Fe-bearing phases are present in the sample, supporting the XRD and SEM data. Otherwise, sextets would have been evidenced below the temperature of ordering. Specifically, the presence of chromite, a presumed catalyst of H_2 generation during serpentinization (Neubeck et al., 2011), would have been revealed during 6K acquisitions since the transition temperature of ordering occurs around 70K (Lodya et al., 1994). Similarly, superparamagnetic magnetite, typically sized <50 nm and formed during early stages of serpentinization (Maffione et al., 2014), presents a doublet at 295K and a sextet at 6K (Wareppam et al., 2022). Although the S1 spectrum acquired at 6K appears similar to the one acquired at 295K, it shows some differences. The two Fe^{2+} contributions of olivine and the Fe^{3+} contribution of Cr-spinel are still successfully fitted at 6K. On the contrary, only one Fe^{2+} contribution of pyroxene is resolved, which could be associated with an unresolved bump at around 4 mm/s that possibly corresponds to a shift in the hyperfine parameters of the missing Fe^{2+} contribution of pyroxene.

Significant changes are observed at low temperature for S2–S5 samples, mainly associated with the multiplication of magnetite contributions that result from the higher ordering of Fe and rearrangement of electron distribution in the mineral lattice. Numerous studies in the literature have, with varying degrees of success, focused on decomposing the MS signal of magnetite into several contributions, with up to 6 subspectral sextets (e.g., García and Subías, 2004). Recently, a study demonstrated the efficiency of considering four contributions to fit low temperature magnetite spectra (Řezníček et al., 2017): one contribution for $8(Fe^{3+})_A$, one for $8[Fe^{3+}]_B$, one for $5[Fe^{2+}]_B$ and one last for $3[Fe^{2+}]_B$. Following this methodology, the S2–S5 spectra were processed by imposing four sextets. The resulting fittings of the external peaks of the S2–S5 spectra appear acceptable, though not as accurate as at 295K. This lies in the multiplicity of magnetite sextets that overlap at 6K and involve large gaussian-shaped peaks. This highlights a difficult deconvolution of MS spectra and uncertain MS data processing for low temperature acquisitions without a strong *a priori* knowledge of the samples. For instance, a complementary magnetic phase in addition to magnetite (e.g., another Fe-oxide), might have been more easily hidden by all other contributions at 6K than 295K. This observation demonstrates the necessity to realize pre-Mössbauer analyses and raises the question of the relevance of performing low temperature MS analyses for the purpose of bulk rock sample characterization. For S1–S4, the same doublets as for 295K spectra were fitted. On the contrary, the multiplicity of magnetite contributions prevented to converge towards a solution with three biotite contributions for S5, giving access only to two of them (Fig. 3j). Once again, this strongly shades the efficiency of low-temperature MS analyses, as it hides other contributions and complexifies the fitting.

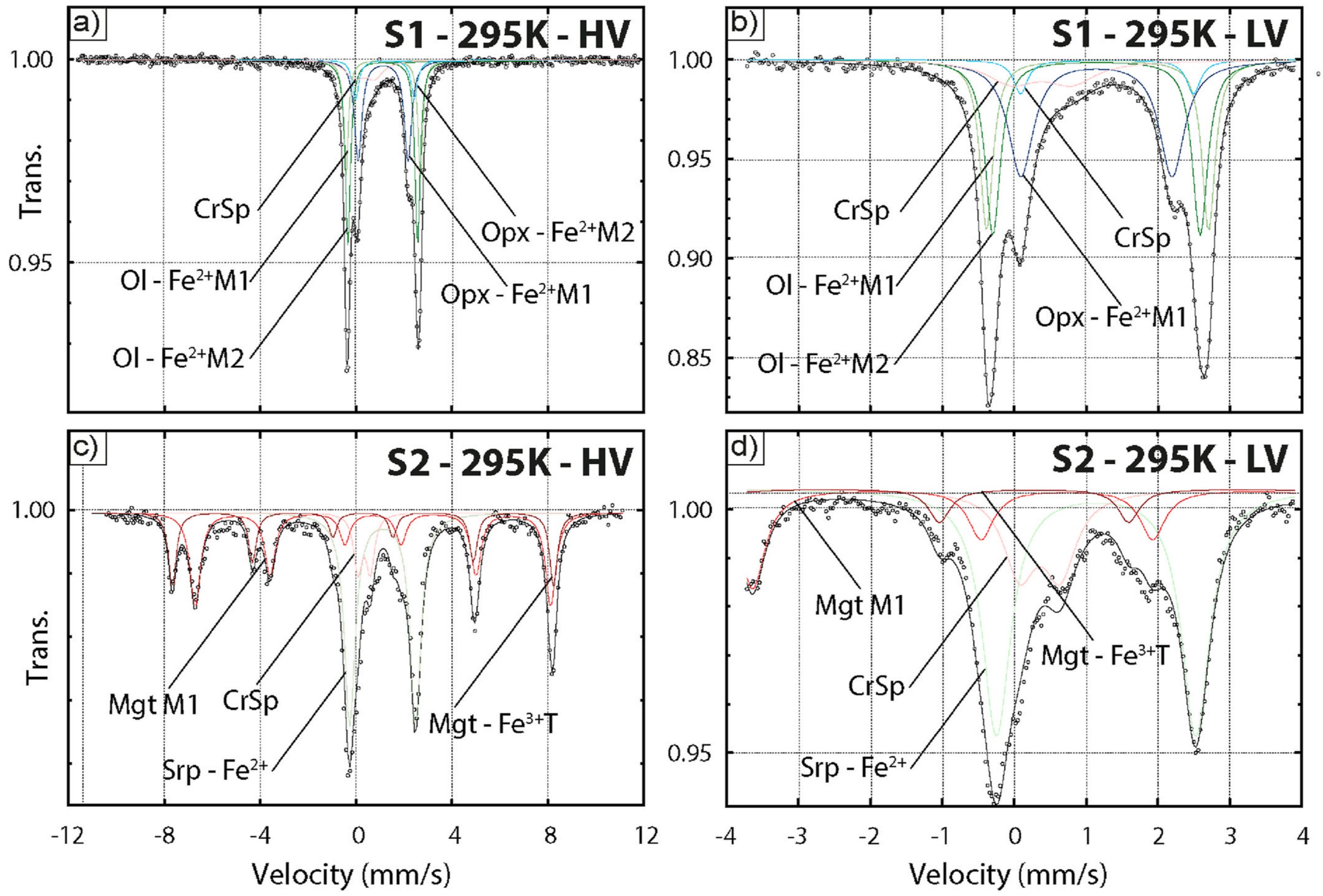

Fig. 4. MS spectra fitting of S1 and S2 samples, for data acquired at room temperature in (a,c) high velocity and (b,d) low velocity. The χ^2 is provided for each fit in Appendix A9. Dots correspond to the raw data and the black line to the fitting result. The comparison highlights the relevance of low-velocity acquisitions when the sample does not contain Fe-oxides, both to save time and improve velocity resolution, allowing for the detection of additional Fe contributions. Conversely, working on low-velocity acquisitions when ferromagnetic phases constitute the sample can involve a loss of precision since the sextets are badly resolved and truncated. Fe occupies either octahedral sites (M) and/or tetrahedral sites (T) in silicate and oxides. CrSp refers to Cr-spinel, Mgt to magnetite, Srp to serpentine, Opx to orthopyroxene, Ol to olivine. For more quantitative information regarding the relative areas of each subspectrum, see section 4.3.

4.2. About the relative relevance of low-velocity acquisitions

The acquisition of MS spectra within a wide range of source velocities (i.e., high-velocity spectra, labeled HV) as presented in the previous section provides access to the full spectrum of sextets associated with magnetic phases. This consequently involves a loss of resolution to accurately fit the doublets, which may necessitate an acquisition in a small range of source velocities (i.e., low-velocity acquisition, labeled LV). The benefits and disadvantages of working on HV and LV spectra are discussed through the meaningful comparison of HV and LV data collected at room temperature for samples S1 and S2.

For S1, the HV spectrum, as discussed previously (Figs. 3a and 4a), exhibits no sextet. It demonstrates that the sample does not carry any magnetic phase. Two olivine Fe^{2+} doublets, two pyroxene Fe^{2+} doublets, and one Cr-rich spinel Fe^{3+} doublet are successfully fitted. In parallel, the fitting of the LV spectrum interestingly displays an important gain in resolution although not revealing any additional contribution compared to the HV spectrum (Fig. 4b). The relative gain in resolution may thus appear useless since it does not help reveal other Fe contributions. Yet, the use of LV acquisitions instead of HV acquisitions can be seen as a time-effective way to perform MS analyses in non-ferromagnetic bearing samples, since it reduces the time of acquisition threefold from velocity source from −4 to 4 mm/s to velocity source from −12 to 12 mm/s).

The relevance of performing such LV acquisitions on magnetic phase-bearing samples is also arguable. For example, the HV spectrum of S2 was previously fitted at room temperature with two magnetite sextets (Fe^{3+} and Fe$^{2.5+}$), as well as one doublet from serpentine Fe^{2+} and one from Cr-rich spinel Fe^{3+} (Fig. 4c). In LV, the gain in resolution brings more difficulty to fit the spectrum (Fig. 4d). Although its shape presents more details suggesting that additional contributions can be fitted compared to the HV spectrum, this task remains impossible due to the poor constraining of contributions from the magnetite sextets. In this example, the LV acquisition alone appears irrelevant. However, one intermediate solution might be to acquire the HV spectrum and process it to properly constrain the hyperfine parameters of sextets, before diving into a more detailed analysis by subsequently acquiring and processing a LV spectrum with the hyperfine parameters obtained from the HV spectrum fitting.

4.3. Quantification of Fe distribution and speciation from MS analyses

Following the qualitative fitting of all spectra, the respective contributions of each Fe (at%) were straightly estimated by considering the relative area of each subspectrum (available in Appendix A9). It may be considered more rigorous to calculate the respective contributions by correcting the relative areas from the recoilless factor (*f*) of each type of Fe. This factor corresponds to the variability between radiation absorption by iron from one to another, depending on its mineral lattice configuration. For instance, tetrahedral Fe^{3+} in magnetite absorbs at room-temperature 6 % more radiations than octahedral Fe$^{2.5+}$, with a f_{octa}/f_{tetra} ratio = 0.94 that can usually lead to an underestimate of Fe$^{2.5+}$ in the magnetite lattice (Sawatzky et al., 1969). The choice not to consider the recoilless factors to further refine the quantification in our samples was primarily led by the high variability in factors displayed in the literature for some minerals (e.g., biotite). This can be explained by the intrinsic variability in Fe environments in the mineral lattice for one single mineral (Dyar, 2002), and can further bias the final quantification by choosing an incorrect factor.

Fe distribution and Fe speciation into the samples are displayed in Table 2, except for low-temperature acquisitions of S3 and S4 that were not considered due to the poor reliability of the fitting (visually approximate curve fitting). Regarding S2 and S5, both Fe^{2+}/$\sum$Fe ratios of magnetite (0.38 and 0.36, respectively) appear unrealistic since Fe^{2+}/$\sum$Fe ratio in magnetite cannot exceed 0.33. Importantly, such a result cannot be explained by the recoilless factor (not considered here) because its consideration would involve a higher Fe^{2+}/$\sum$Fe ratio. On the contrary, this highlights the challenge of deconvoluting the respective contributions of magnetite at low temperature (Řezníček et al., 2017), and likely even more while working on complex mineral assemblages. In this context, it is clear that our data fitting was performed using only Lorentzian profiles, which may be less effective at capturing the spectral complexity of natural samples than Voigt profiles (Rancourt, 1994). Specifically, in the case of magnetite in our samples, an inaccurate accounting for distributions in the hyperfine field (arising, for instance, from particle size variability, altered surfaces, defect or cationic substitutions) could contribute to both the apparent non-stoichiometry and imperfect spectral fits. For these reasons, the quantifications of S2 and S5 at low temperature also seem of poor reliability with visually not always accurate curve fitting (see Fig. 3). Altogether, these quantitative results underline that room-temperature analyses should be privileged to characterize bulk rock samples. Regarding high-velocity vs low-velocity acquisitions, our quantifications thus suggest the latest should be avoided if a magnetic phase constitutes the sample, as it involves a bias in the quantification. For samples that do not carry a magnetic phase, LV acquisitions might not change the quantification dramatically but still reduce acquisition time threefold.

4.4. Comparison with titration method and MS error determination

In the literature, the reliability of MS analyses is commonly

Table 2
Fe distribution and speciation in the studied samples, according to the various MS acquisitions and processing performed at 6K and 295K, for radioactive source velocities of ±4 mm/s (LV) and ±12 mm/s (HV). Fe^{2+} * refers to the Fe^{2+}/$\sum$Fe ratios calculated for each mineral and the bulk rock samples and is comprised between 0 and 1. For S3 and S4, Fe distribution was not considered (N.C.) for spectra recorded at 6K due to the extremely poor quality of the fitting (see Fig. 3).

Sample	Ol		Opx		Serp		Cr-Spn		Mgt		Fe-carb		Bi		Bulk	
	%at	Fe^{2+} *	%at	Fe^{2+} *	%at	Fe^{2+} *	%at	Fe^{2+} *	%at	Fe^{2+} *	%at	Fe^{2+} *	%at	Fe^{2+} *	%at	Fe^{2+} *
S1-295K-HV	54	1.00	35	1.00			11	0.00							100	0.89
S1–295K-LV	52	1.00	36	1.00			12	0.00							100	0.88
S1-6K-HV	57	1.00	31	1.00			12	0.00							100	0.88
S2-295K-HV					40	1.00	8	0.00	52	0.31					100	0.56
S2–295K-LV					33	1.00	12	0.00	55	0.28					100	0.50
S2-6K-HV					35	1.00	8	0.00	57	0.38					100	0.51
S3-295K-HV									87	0.32	13	1.00			100	0.40
S3-6K-HV									N.C.	N.C.	N.C.	N.C.			N.C.	N.C.
S4-295K-HV									76	0.32			24	0.71	100	0.42
S4-6K-HV									N.C.	N.C.			N.C.	N.C.	N.C.	N.C.
S5-295K-HV									55	0.28			45	0.67	100	0.45
S5-6K-HV									67	0.36			33	0.70	100	0.47

estimated by comparison with wet chemistry, i.e., Fe^{2+} titration, notably on single phase MS analyses such as isolated biotite (Dyar, 2002). From the authors' knowledge, such a comparison on bulk rock powder is rare in the literature, if existent. In the present study, we apply this comparison methodology by cross-checking our MS results with the titration results, performed on the same samples. Quantitative results and error bars calculated for each titration are provided in Appendix A3. Due to the uncertainties associated with low-temperature MS spectra fitting and quantifications, as discussed in the previous section, only room-temperature MS data are compared with titrations.

At first sight, the $Fe^{2+}/\sum Fe$ ratios obtained from MS and titrations appear very similar, with crossplots falling very close to the 1:1 ratio curve and displaying a Pearson correlation parameter of $r = 0.96$ (Fig. 5). In more detail, one sample (S4) lies on the 1:1 curve, two others (S1 and S2) overlap the line when considering the titration uncertainty, while the two lasts (S3 and S5) lie farther. Unfortunately, no direct way of quantifying MS uncertainty exists since the sources of error are multiple. It often resides in (i) a contribution drowned in the background noise, (ii) a contribution hidden by another due to overlapping, which can result for instance in a minor Fe^{3+} subspectrum involuntarily incorporated into a predominant Fe^{2+} subspectrum, changing as a consequence the overall $Fe^{2+}/\sum Fe$ ratio, (iii) a wrong choice in selecting hyperfine parameters, that result in a wrong characterization of the sample. Therefore, the comparison with Fe^{2+} titration provides a direct mean to estimate the uncertainty associated with the MS quantification of $Fe^{2+}/\sum Fe$ ratios. The first way of quantifying it is to calculate the deviation between the MS results and the titration results, which corresponds to $+0.03$, $+0.03$, $+0.05$, 0.00, and -0.09 for S1, S2, S3, S4, and S5, respectively (Table 3). Rather than providing a deviation percentage from the titration result, it may be considered more robust to provide a range of minimum and maximum deviation on the MS result, with respect to the titration uncertainty. In that case, the ranges of MS errors are 0 to $+0.08$ (S1), 0 to $+0.06$ (S2), $+0.03$ to $+0.07$ (S3), -0.02 to $+0.02$ (S4), and $+0.05$ to $+0.13$ (Table 3). From these deviation calculations, the reliability of MS results appears high, with an absolute mean deviation of 0.04 and an absolute mean range of deviation of 0.02–0.07.

Digging further into the cross-comparison highlights that three samples show a slight overestimate of Fe^{2+} by MS, or an underestimate of Fe^{2+} by titration (S1, S2, and S3), while one other shows an underestimate of Fe^{2+} by MS, or an overestimate of Fe^{2+} by titration (S5). These deviations, although no definitive explanation can be provided, might rely on one of the following points or a combination of these, discussing the respective titration and MS limitations:

Table 3
Absolute $Fe^{2+}/\sum Fe$ obtained from MS and titration, along with the analytical titration error and the estimated MS error. * In the table, the deviation is given as absolute values, although some of them are positive while others are negative with respect to titration.

Sample	$Fe^{2+}/\sum Fe$ Tit mean	$Fe^{2+}/\sum Fe$ Tit min-max	$Fe^{2+}/\sum Fe$ MS	MS deviation* from mean Tit	MS range of deviation* with respect to titration min-max
S1	0.85	0.80–0.88	0.88	0.03	0 to 0.08
S2	0.53	0.50–0.56	0.56	0.03	0 to 0.06
S3	0.35	0.33–0.37	0.40	0.05	0.03 to 0.07
S4	0.42	0.40–0.44	0.42	0	0.02 to 0.02
S5	0.55	0.51–0.59	0.46	0.09	0.05 to 0.13
			Mean deviation	0.04	0.02 to 0.07

(i) The deviation is due to an inaccurate $Fe^{2+}/\sum Fe$ estimate during the titration. The difficulty in accurately quantifying Fe^{2+}, representative of the bulk sample digested, has been the subject of numerous studies. Two main challenges are usually encountered. First, the complete dissolution of the bulk sample can be difficult, as certain types of Fe-bearing minerals require stronger reagents than others such as poorly reactive sheet silicate (Hepburn et al., 2020). In the present study, the choice of using $HF–H_2SO_4$ was made tentatively to prevent any incomplete dissolution of the bulk sample and, especially, of the sheet silicate (Anastácio et al., 2008) However, this possibility cannot be ruled out. Second, the acid-titration has been reported to induce artifacts of Fe oxidation or reduction. Indeed, artificial Fe oxidation during chemical reaction remains possible despite all precautions taken during the dissolution and titration processes, as no specific apparatus ensuring a complete oxygen exclusion was used (Xue et al., 2017). Another concern is the destabilization of sulfide minerals such as pyrrhotite or pyrite, introducing S^{2-} in the

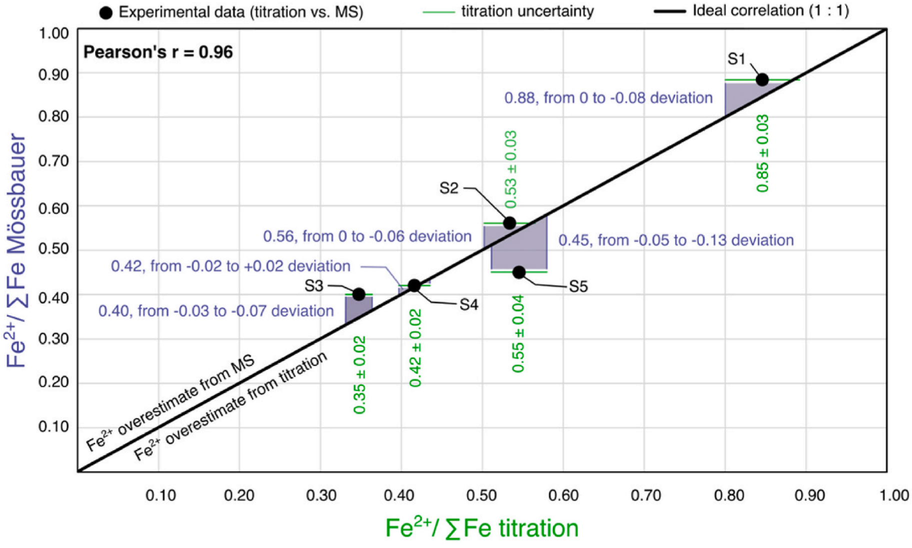

Fig. 5. Cross-comparison of $Fe^{2+}/\sum Fe$ results obtained from MS and titration analyses on the five studied samples. The green color refers to titration results and associated analytical errors, and the blue color to MS results and estimated errors. Since no straight methodology exists to calculate uncertainty on MS quantification, it can be estimated by calculating the deviation between MS results and titration results. (For interpretation of the references to color in this figure legend, the reader is referred to the Web version of this article.)

media that will likely reduce Fe^{3+} into Fe^{2+} to form S^0 precipitates (Husler et al., 2011). Regarding this point, none of the studied samples presents significant amounts of sulfide minerals (see Table 1), thus suggesting no artifact of such type. More precisely, only S1 revealed minor amounts of pyrite, and the $Fe^{2+}/\sum Fe$ quantification obtained by MS fall within the titration uncertainty range (the error bars cross the 1:1 curve in Fig. 5).

(ii) The deviation is due to an inaccurate MS spectrum deconvolution. Several algorithms exist to fit MS data, that lay on different mathematic concepts and can occasion a certain variability in the quantitative results (Dyar et al., 2006).

(iii) The deviation is due to the various recoilless factors that have not been considered to correct the relative contributions of each Fe in our samples from their relative subspectrum surface areas. Data available in the literature suggest that these factors are lower for Fe^{2+} than Fe^{3+} whatever the mineral, involving an increase of $Fe^{2+}/\sum Fe$ ratio of the sample when recoilless factor corrections are made. Therefore, such a correction could explain the deviation observed for S5, which shows an underestimate of Fe^{2+} by MS. It is, however, unlikely since it would then involve a concomitant increase of MS deviations for the 4 other samples, for whom MS quantifications are already in equilibrium or slightly overestimated in Fe^{2+} with respect to titrations.

(iv) The deviation is due to Fe contributions in the samples, that are invisible in high-velocity MS spectra. On the contrary to S1, S2 (MS deviation within titration uncertainty), and S4 (MS in equilibrium with titration), S3 and S5 exhibit a positive and negative MS deviation, respectively. These deviations, which signify an overestimate and underestimate of Fe^{2+} respectively, qualitatively correlate the findings of minor amounts of hematite (ideal formula: $Fe_2^{3+}O_3$) in S3 and ilmenite (ideal formula: $Fe^{2+}TiO_3$) in S5 that could explain these deviations. In the specific case of S5, ilmenite exhibits a doublet that could be easily hidden in the complexity of the inner part of the spectra (Fig. 3e). As such, an additional LV acquisition may help gain resolution and get insight to validate or invalidate this assumption.

4.5. *Strengths and limitations of MS for studying Fe-rich H_2-generating rocks and beyond*

In Earth Sciences, the use of MS has been highly focused historically on the characterization of natural single phases (De Grave and Vochten, 1985; Dyar, 2002; Lodya et al., 1994; McGuire et al., 1991; Vandenberghe and De Grave, 1989). More recently, MS gained much interest in fundamental and applied Environmental Sciences where applications developed to characterize synthetic experimental materials as well as complex natural soils (Chen et al., 2023; Gorski and Scherer, 2009; Latta et al., 2012; Notini et al., 2023; Thompson et al., 2006). Our study demonstrates that MS is also a powerful tool to characterize iron in complex natural rock samples. Our MS quantification results, only based on first-order quantifications, align well with the titration results, with estimates of $Fe^{2+}/\sum Fe$ ratio only deviating by 0.04 on average (see section 4.4 for the related discussion). Unlike titration, it additionally provides major insights on iron mineralogy.

This outcome carries interesting perspectives in the field of fundamental geology. For instance, $\sum Fe$ in bulk samples and minerals has long been routinely measured only using microprobe, and is often considered as Fe^{2+} for simplicity. However, the $Fe^{2+}/\sum Fe$ ratio is now recognized as a key parameter for calculating effective geothermometers and modeling phase equilibrium (Forshaw and Pattison, 2021; Inoue et al., 2018). A widespread use of MS may help reevaluate many past studies by considering the $Fe^{2+}/\sum Fe$ ratio. Meanwhile, in applied geology, the development of MS could be a game-changer for the exploration and characterization of raw resources, such as iron ores or H_2-generating rocks. The economic exploitability of an iron ore largely depends on its grade, i.e., its Fe content, speciation, and mineralogy. The widespread use of MS through an effective workflow may positively impact iron-ore exploration programs by reducing the analytical time required for iron-ore characterization. Regarding the potential of H_2-generating rocks, the kinetics of generation, and the P-T conditions to generate H_2 have been recognized to depend on the total budget of Fe^{2+} in the lithology as well as the mineral carrying this budget (Klein et al., 2013). As such, our characterizations of S1 and S2 provide a meaningful example of the effectiveness of MS. Studies highlighted that Fe^{2+}-serpentine (for instance S2 type rocks) is prone to generate H_2 below 100 °C (Ellison et al., 2021), although this mineral is known to remain stable at higher temperature (Klein et al., 2013). Conversely, experimental studies highlighted that the H_2 generation rate from olivine (for instance S1 type rocks) is dramatically reduced at lower temperatures, decreasing a thousandfold from 300 °C to 200 °C. Therefore, it is of major interest to quantify not only the bulk $Fe^{2+}/\sum Fe$ ratio (e.g., by titration) and mineralogy (e.g., by XRD), but also the specific distribution of Fe^{2+} in samples (e.g., by MS) , as it is expected to involve different pathways for H_2 generation.

Altogether, this study also raised limitations regarding the use of MS, that are worth to frame for a conscious and efficient utilization. As discussed below, it is clear that all these limitations can be addressed by performing complementary analyses, which are often time-consuming and mostly conducted at the micrometric scale, raising the question of representativeness. It is up to the operator to balance the pros and cons of complementing MS analyses with additional characterization methods, depending on the desired level of precision. These limitations can be broadly divided into four categories:

(i) MS analyses performed on bulk rock samples inhibit the detection of minor Fe-contributions in the sample (as discussed earlier, especially for S3 and S5), since their signal is drowned into the others. This limitation can somehow be neglected in the framework of H_2-generating rock characterization, if one considers that the H_2 potential of a rock resides in the dominant Fe contributions and not in minor ones. Additional SEM observations may, however, be undertaken to evaluate the presence of these minor contributions.

(ii) The respective Fe-contributions obtained from the deconvolution of the different subspectra are averaged for each mineral species. In other words, this technique does not allow to distinguish different generations of the same mineral, bearing different chemistries. As such, the use of this technique should be limited to the determination of the H_2-generating potential of rocks and not extended to the fine study of the history of the sample. For instance, the pre-MS petrographic inspections performed on S2 highlighted different generations of serpentinization episodes, that cannot be evidenced using MS. There, on possible solution might be to conduct XANES analyses, that provide in-situ assessments on $Fe^{2+}/\sum Fe$ ratio in micrometric spots, allowing to constrain the respective $Fe^{2+}/\sum Fe$ ratio of different generations of the same alteration mineral (Combaudon et al., 2024).

(iii) This technique only provides information on the Fe-distribution and Fe-speciation in the sample but does not provide a quantification of Fe content in the studied sample. Thus, a complementary analysis such as acid-digestion and titration of $\sum Fe$ may be performed to quantify the total Fe-budget.

(iv) Finally, the H_2-generating potential of Fe-rich rocks does not only depend on the Fe-content, Fe-distribution, and Fe-speciation. It is also dependent on the presence of mineral or chemical catalysts and inhibitors of reactions such as chromium, aluminum or nickel (Andreani et al., 2013a; Mayhew et al., 2013), that cannot be investigated through MS. Regarding this last point, although MS must hold a central place in the characterization of H_2-generating rocks, it must be completed by subsequent analyses and ICP-OES analyses on bulk samples seem convenient.

4.6. Using MS in an efficient workflow for H_2-generating rocks characterization

This study demonstrates that MS has the potential to serve as a key tool for characterizing the H_2-generating potential of (Fe-rich) rocks. Especially for natural H_2 prospection, its use may drastically shorten the number of techniques required to characterize drill cores that come back from drillings. Consequently, it would also reduce the time required for a full sample characterization. A MS acquisition and processing can be performed within 1–2 days (depending on Fe-content) without too specific sample preparation and provides a full batch of information, while other conventional techniques such as XANES provide only very specific insights and require time-costly sample conditioning like FIB-section preparation (usually several weeks required for the whole analytical chain). However, to maximize the benefits of this technique, it must be applied judiciously and integrated into a short and optimized sequence of analyses (Fig. 6).

MS requires prior knowledge to accurately interpret the acquired spectra, and must be preceded by mineral characterization. In this study, pre-MS characterization was conducted using both microscopy and XRD. However, these techniques are time-consuming and do not meet the need for rapid characterization of H_2 exploration campaigns. Instead, we propose the use of hyperspectral mineral mapping of raw drill cores returned from the field, a non-destructive and efficient technique that has been employed successfully in the mining industry for decades, to quickly identify mineralized veins (Contreras Acosta et al., 2021; Schodlok et al., 2016). Once this mapping is completed, MS analyses can follow. As demonstrated in this study, 295K and 6K acquisitions present intrinsic limitations. At 295K, it may be necessary to apply a recoilless factor correction to achieve more accurate quantifications, while at 6K, there is difficulty in properly fitting all the magnetite contributions below the Verwey transition. These two extreme temperatures were investigated being aware that an intermediate temperature may be more suitable for characterizing H_2-generating rocks. For those analyzing magnetite-bearing samples and having access to low-temperature cryostats, acquisitions at 140K may be ideal, as it would remain above the Verwey transition (thus only requiring fitting two magnetite sextets) and be cool enough to negate the need for recoilless factor corrections (Gorski and Scherer, 2010). For those who do not have access to low-temperature cryostats, room-temperature acquisitions should be privileged, as the spectral fitting is simplified but sufficient enough to get relatively accurate $Fe^{2+}/\Sigma Fe$ estimates. In fact, the cross-comparison between room-temperature MS and titration results realized in this study confirms that MS is a reliable technique for assessing $Fe^{2+}/\Sigma Fe$ ratios, with an average deviation of 0.04, and without considering any recoilless factor correction that is debated in the literature. For a more precise and confident estimate, applying these corrections could be beneficial, but it presents challenges since not all recoilless factors are well-constrained. Additionally to high-velocity acquisitions, low-velocity acquisitions may be relevant in some cases to increase resolution and better constrain the doublets. Spectral fitting should be performed intelligently, based on the initial mineral characterization to avoid misinterpretation. Finally, refining the H_2-generating potential of the most promising rocks will likely require further characterization of elemental contents, such as Ni and Al, which act as chemical catalysts in H_2 generation (Andreani et al., 2013a; Barbier et al., 2020; Sissmann et al., 2013).

It is important to emphasize that this study, and the resulting workflow presented earlier, aim to promote the broader use of MS as a time-effective tool for characterizing Fe-bearing rocks in the context of natural H_2 exploration, even for non-MS specialists. For that reason, the focus was placed on traditional transmission-mode MS analyses on bulk powders, which represent the most common and accessible approach for actors in the exploration field. However, a wide range of analytical protocols based on the Mössbauer effect have been developed and may be useful for those seeking to exploit further the MS-related techniques. In particular, significant progress has been made over the years in terms of radiative source design and beam size. As extensively detailed by McCammon (2021) and references therein, conventional ^{57}Co sources are optimized for analyzing samples as small as 2 mm in diameter, which is well-suited for bulk analysis but limits the ability to analyze individual mineral grains or very fine particles separately. To address this limitation, higher-activity point-sources (i.e. sources with greater ^{57}Co concentrations at first order) have been developed, enabling the analysis of samples down to approximately 100 μm. Taking this miniaturization even further, synchrotron-based Mössbauer spectroscopy has been established at several facilities, offering high-intensity beams that allow spatial resolutions as fine as 30 μm, with acquisition times as short as few minutes (instead of several hours for point-sources and several days for conventional sources). Ultimately, selecting the optimal MS source

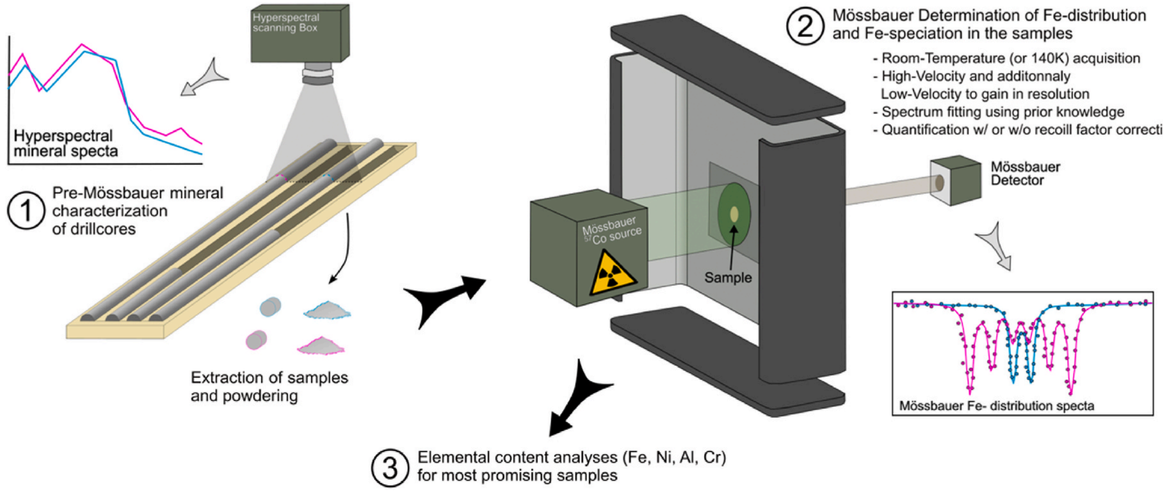

Fig. 6. Schematic view of the place of Mössbauer spectroscopy (MS) in an automatized and routinely-operated Fe-rich rock characterization, in the framework of H_2 prospection. This work demonstrates that MS acquisitions should be privileged at room-temperature (or 140K, see discussion), in high-velocity. No consensus exists on the necessity to correct the MS raw quantifications at room-temperature by the recoilless factor, and it should be thus avoided. A quality MS spectrum fitting requires prior knowledge of the sample mineralogy, for instance fast and non-destructive hyperspectral mineral analyses. MS should be performed afterward. To refine the estimate of the H_2-generating potential of the samples, elemental analyses should be further performed to track the presence of any possible chemical catalyst.

involves trade-offs between sample size and Fe-content, acquisition time, and cost. Another significant MS development has been made in parralel to the traditional transmission mode (i.e. based on detecting absorbed γ-rays during nuclear excitation), consisting in operating in backscatter mode (i.e. based on detecting γ-rays re-emitted during nuclear de-excitation). Among its advantages, this mode requires no sample preparation and can be applied directly to cohesive surfaces such as drill cores. It provides reasonably deep penetration, up to ~200 μm in cohesive materials and up to ~2 mm in fine-grained powders, thereby enhancing the representativeness of the analysis (see Klingelhöfer et al. (2003) and references therein). Therefore, the backscattered MS approach may offer significant time savings for H_2-generating rock characterization.

5. Conclusion

For H_2 prospection, actors will have to find time-saving and efficient solutions to assess the past or present H_2 generation from Fe-rich rock samples, as well as their remnant potential. Up to now, these questions have been addressed through (i) time-consuming microscale characterization methods that raise the question of the representativeness of the results at the bulk scale, or (ii) quicker bulk rock sample characterization methods that raise the question of their precision.

In this study, we used MS to determine the distribution and speciation of Fe in powdered materials, coming from five samples containing varying amounts of Fe^{2+} and different Fe-bearing minerals. The key finding is that, with an appropriate acquisition setup (room-temperature, high-velocity) combined with prior mineralogical knowledge, MS data processing can yield meaningful results comparable to those obtained through conventional titrations. Importantly, the MS provides access to the various iron-bearing mineral phases. This knowledge is essential, as the H_2 generated by redox reactions can be associated with different Fe minerals, and therefore at various temperature and depths.

Our study shows that the MS could become a key tool in natural H_2 prospection. This study provides strong evidence that Mössbauer spectroscopy can be integrated into a simplified sequence of analyses, significantly reducing the time required for rock characterization by replacing more time-consuming methods such as microscopy. While it is commonly employed to study iron in individual minerals, our results show that MS can be used on complex mineral assemblages, and without applying second-order corrections (e.g., recoilless factor). Finally, we propose a sequential approach to assess the most critical parameters for evaluating the H_2-generating potential of rocks: bulk mineralogy (hyperspectral imaging), bulk Fe-distribution and Fe-speciation (Mössbauer spectroscopy), and bulk iron and catalyst content (elemental analyses).

Funding

This work is part of the PhD projects of UG, funded by MERSI and INSU-CNRS (TelluS), and KL, funded by ANRT through the CIFRE Project and the Nouvelle-Aquitaine region through the H2NA Project.

CRediT authorship contribution statement

U. Geymond: Writing – original draft, Visualization, Software, Methodology, Investigation, Formal analysis, Data curation, Conceptualization. **K. Loiseau:** Writing – original draft, Visualization, Software, Methodology, Investigation, Formal analysis, Data curation, Conceptualization. **V. Roche:** Writing – original draft, Visualization, Methodology, Investigation, Formal analysis, Data curation, Conceptualization. **G. Pasquet:** Writing – original draft, Visualization, Methodology, Investigation, Formal analysis, Data curation, Conceptualization. **S. Revillon:** Writing – original draft, Visualization, Investigation, Formal analysis, Data curation, Conceptualization. **M. Sougrati:** Validation, Supervision, Formal analysis. **I. Moretti:** Writing – original draft, Validation, Supervision, Funding acquisition, Conceptualization.

Declaration of competing interest

The authors declare that they have no known competing financial interests or personal relationships that could have appeared to influence the work reported in this paper.

Acknowledgments

All authors are grateful to Charles Aubourg (UPPA) for his support and for accompanying this study with great interest, Sophie Nowak (UPC) for performing XRD analyses and for further help on data interpretation, Stephan Borenstjan (IPGP) for his assistance during SEM sessions, Andrew Grigg (ETHZ) and Denisa Kubaniova (Univ. Praha) for Mössbauer spectra acquisitions and always insightful discussions.

Appendix B. Supplementary data

Supplementary data to this article can be found online at https://doi.org/10.1016/j.apgeochem.2025.106399.

Appendices.

Appendix A1. Overview of the Mössbauer Spectroscopy technique to support the comprehensibility of this study for non-Mössbauer specialists

Theory on the Mössbauer effect

The Mössbauer effect has been extensively studied and discussed in a wide range of literature reviews (Stevens et al., 2005; Yoshida and Langouche, 2013). This section provides a summary to support the comprehensibility of the present study and is based on the pre-existing literature on Mössbauer Spectroscopy (Dyar et al., 2006; Grandjean and Long, 2021; Murad, 2010; Stevens et al., 2005; Yoshida and Langouche, 2013). For a given isotope (in our case ^{57}Fe), the Mössbauer effect consists in the absorption of energy, γ-ray, that slightly differs from the theoretical energy gaps of electron transitions. Such an effect originates from interactions between the ^{57}Fe atom electronic shell and its close environment such as the speciation of Fe or the nature of the mineral lattice embedding the atom. The shifts in energy are defined by the so-called hyperfine parameters (detailed below). These shifts can easily be evidenced by changing the velocity of the γ-ray source irradiating the material (expressed in mm/s), which results in a change of frequency and thus the energy of γ-rays according to Planck's relation. Since hyperfine parameters are characteristic of each atomic configuration, the study of absorption patterns provides a powerful tool to determine the Fe environment in a specific lattice. Non-ferromagnetic materials generally exhibit a doublet spectrum (Figure A1a), visible in the low-velocity acquisitions (Low-V, source velocity from −4 to 4 mm/s). The doublet is described with three hyperfine parameters, namely the isomer shift (IS or δ_{Fe}), the quadrupole splitting (QS or ΔE_Q) and the full width at half maximum (FWMH or Γ) (Figure A1b). Conversely, magnetic material exhibits a doublet spectrum above the ordering temperature and generally a sextet below this threshold temperature, once the material is magnetically ordered (Figures A1c and A1d). It is common to perform analyses on magnetic materials, for instance, some amphiboles, at various temperatures to characterize more accurately Fe distribution within the material and constrain the ordering temperature (Van Alboom and De Grave, 1996). Three hyperfine parameters are mandatory to describe the shifts in energy of iron carried by magnetic materials, the (δ_{Fe}), the quadrupole shift (2ϵ), and the magnetic hyperfine field (H_f). In comparison with the doublets, the sextet spans over a wider range of velocity sources, which require high-velocity spectra acquisitions (High-V, source velocity from −12 to 12 mm/s), but appear then very convenient to evidence the presence of oxides.

Qualitative and quantitative determination of Fe distribution

From a practical point of view, the Mössbauer spectrum of a studied sample results from the sum of all the subspectra of the various types of Fe present. As such, deciphering the various subspectra allows to get semi-quantitative information about Fe-distribution and Fe-speciation within the sample. Unfortunately, achieving a high-quality Mössbauer spectrum fitting is often difficult when working with complex materials such as natural samples, where all the subspectra overlap themselves. At least two leverages can be used to mitigate this limitation. First, a wise choice of the relevant parameters, predominantly temperature, and width of spectrum acquisition, must allow a gain in resolution and better fits of the respective contributions. Second, a lot of studies (e.g. Fukuyama et al., 2022; Sommerfeld and Friedrich, 2022; Winsett et al., 2019) devoted to constraining Fe-mineralogy in natural samples attached their effort to separate each mineral and analyze it by MS independently, which increases precision drastically. One may argue, however, that a good *a priori* knowledge of the sample is sufficient to accurately decipher the respective contributions of each Fe within the bulk sample. Regarding the quantification of the relative contributions, each subspectrum area provides, in first order, the respective abundances of the different types of Fe present in the sample. Further corrections can be applied to refine the quantifications, e.g. the recoilless factor.

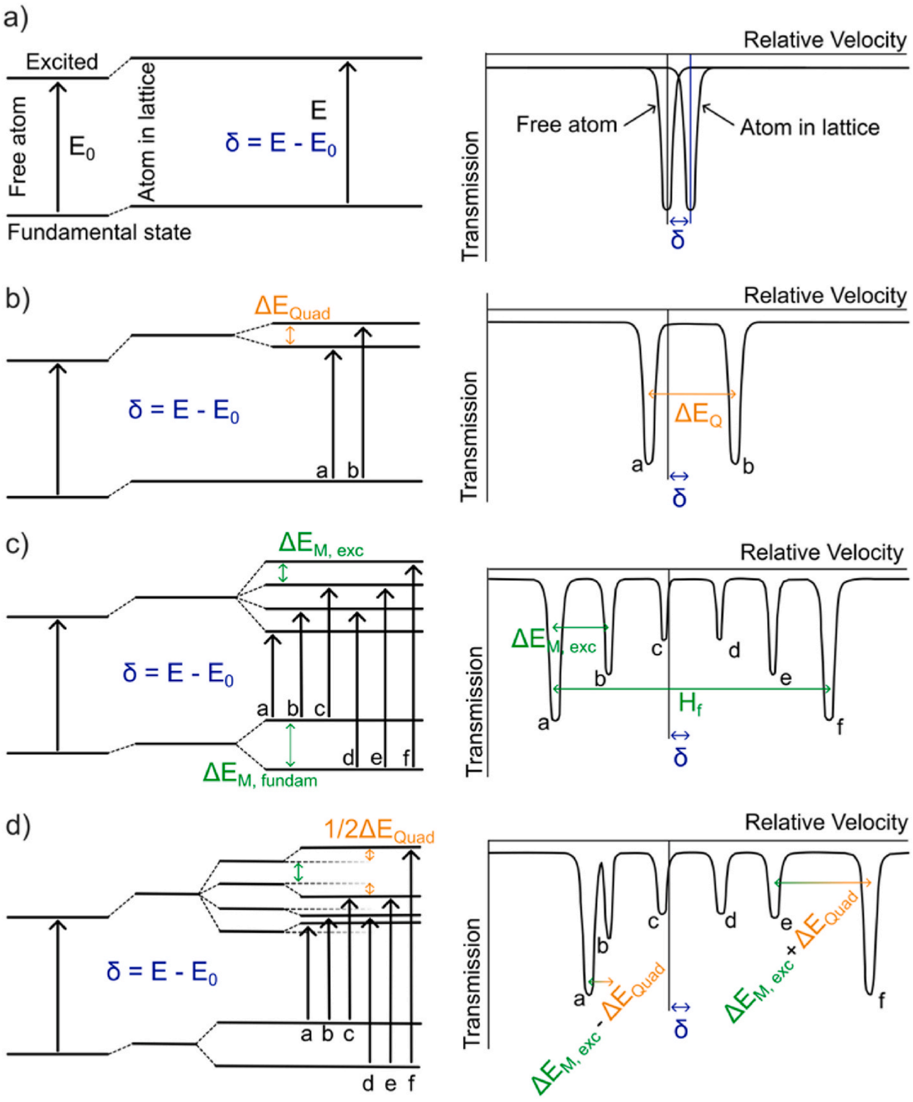

Fig. A1. Simplified view of the dependency of hyperfine parameters on the Mössbauer effect and associated spectra for magnetic and non-ferromagnetic Fe-bearing material. For doublets, the morphology is defined by (a) the isomer shift δ_{Fe} and (b) the quadrupole splitting ΔE_Q. For sextets, the morphology is controlled by a third parameter, (c) the hyperfine magnetic field (H_f). It results in a complex signal where all hyperfine parameters influence the shape of the spectra. Please note that 8 γ-transitions are expected in theory but only 6 are evidenced for ^{57}Fe. For more details refer to (Yoshida and Langouche, 2013).

Appendix A2. Additional characterization methods

Bulk sample mineral compositions involved X-ray diffraction (XRD) analysis using a Malvern-Panalytical® Empyrean diffractometer equipped with a copper tube (Kα = 1.541874 Å) and a Malvern-Panalytical® multi-channel PIXcel detector (UPC, Paris). The experimental setup included an angular range between 5° and 80°, with a step size of 0.007° and a time per step of 80 s, resulting in a total measurement time of 1 h per sample. Data interpretation was facilitated using Highscore Plus software from Malvern-Panalytical®.

To ensure the reliability of the X-ray diffraction results, scanning electron microscopy observations were done using a Zeiss® Auriga40 microscope. The microscope was equipped with a 1 nm resolution field emission gun and a Bruker® Quantax 800 energy-dispersive X-ray spectroscopy feature, complemented by a Bruker® XFlash 410-M detector.

Bulk sample elementary compositions were analyzed by Inductively Coupled Plasma Atomic Emission Spectrometer using a Horiba Jobin Yvon Ultima 2, following the protocol adapted from (Cotten et al., 1995). Each powdered sample was digested in Teflon vials with HF 32 N and $HNO_3$14.4 N, and the resulting dry residue was dissolved in a H_3BO_3 solution. Mica-Fe and IF-G international standards served as internal and external control. Typically, measurements conducted on this instrument exhibit a precision better than 4 % for concentrations exceeding 1 %.

Iron speciation ($Fe^{2+}/\sum Fe$ ratios) in the samples was determined through $KMnO_4$ titration of FeO after a HF + H_2SO_4 dissolution, following a method modified from Jen (1973) and Teagle (1993). For each sample, 0.5 g was carefully weighted. 8 ml of 1:1 H_2SO_4 and 5 ml of 32 N HF were added to the sample in polypropylene bottles and left to digest for a minimum of 20 mn in a simmering water bath. Once the digestion step was completed, the sample was transferred to a beaker for titration following HF neutralization by boric acid. Titrations on the studied samples were replicated to ensure the reproducibility of the results. The mean value is provided in the results table in Appendix A3. Uncertainties were evaluated by replicating several times analyses of 3 different sorts of standard material of known FeO concentrations. The deviation between the measured and the expected FeO concentrations was then calculated. Empirically, the error on the measurements was found to depend on the FeO concentrations, which emphasizes the loss of precision of the method when the sample becomes less concentrated in iron, following a power law relationship presented below: Error (%) = $0.05[\text{FeO (wt\%)}]^{-0.624}$ (Figure A2). For instance, this law imposes a 1.2 % uncertainty for samples containing 10 wt% of FeO.

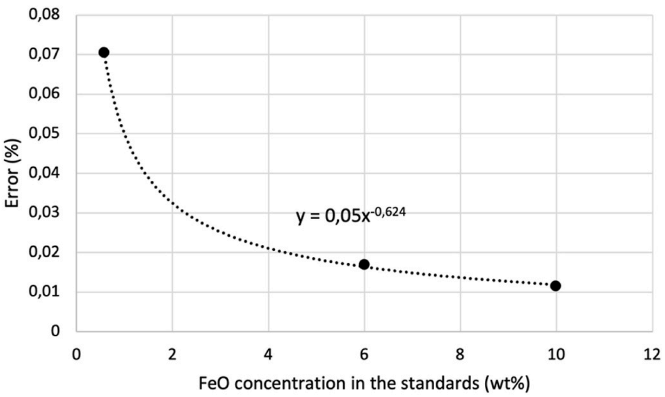

Fig. A2. Error on Fe^{2+} titration of standards, depending on FeO concentrations in the standards. Error corresponds to the SD, calculated after several analysis replications.

Appendix A3. Raw results of elementary analyses (ICP-OES) and iron titration performed on the samples, allowing determination of $Fe^{2+}/\sum Fe$ ratios in the respective samples

Table A1

Raw results of elementary analyses (ICP-OES) and iron titrations performed on the samples. Fe_2O_3* refers to Fe_2O_3 total. The estimated uncertainties for iron ICP-OES analyses and titrations are given in parenthesis, and correspond to a percentage of the value. For more details on the quantification methods, refer to Appendix A2. The errors on $Fe^{2+}/\sum Fe$ ratios are provided in parenthesis and calculated following the rules of uncertainty propagation.

Sample	ICP-OES (wt%)												Titration (wt%)	$Fe^{2+}/\sum Fe$
	SiO_2	TiO_2	Al_2O_3	Fe_2O_3*	MnO	MgO	CaO	Na_2O	K_2O	P_2O_5	LOI	Total	FeO	
S1	44.00	0.12	2.01	8.51 (4)	0.12	41.18	3.18	0.31	0.05	0.02	2.01	101.51	6.50 (1.6)	0.85 (5.6)
S2	39.84	0.09	2.44	7.87 (4)	0.11	38.31	1.99	0.14	0.06	0.02	10.48	101.36	3.83 (2.2)	0.53 (6.2)
S3	39.20	0.10	1.70	52.90 (4)	0.84	2.17	0.69	0.03	1.41	0.48	4.21	103.75	16.54 (0.9)	0.35 (4.9)
S4	29.75	0.50	8.55	49.59 (4)	0.17	4.30	1.10	0.13	4.27	0.80	0.00	99.16	18.56 (0.8)	0.42 (4.8)
S5	66.03	0.71	12.03	6.82 (4)	0.03	1.52	1.90	2.29	5.50	0.22	1.62	98.68	3.35 (2.4)	0.55 (6.4)

Appendix A4. Abacus of Mössbauer hyperfine parameters of some key minerals studied for H_2 generation

Table A2
Abacus grouping room-temperature hyperfine parameters at of multiple mineral phases of interest for H_2 exploration, according to data available in the literature. Contrib* corresponds to the christallographic site incorporating Fe and is most of the time octahedrally (M) or tetrahedrally (T) coordinated in the mineral lattice. Additional informations can be found in the related references, listed as followed: (1) Dyar et al. (2006); (2) McGuire et al. (1991); (3) Doriguetto et al. (2003), (4) Malczewski and Popiel, 2008.

Mineral		Contrib*	Fe valency	δ (mm/s)	QS/ΔEQ (mm/s)	B_{Hf} (T)	Reference
Olivine	$(Fe_x, Mg_{2-x})SiO_4$	M1	Fe^{2+}	1.14–1.18	2.80–3.10		(1),(3),(6)
				1.15–1.18	3.07–3.09		
		M2	Fe^{2+}	1.13–1.16	2.83–2.91		(6)
Almandine	$Fe_3^{2+}Al_2(SiO_4)_3$	dodec	Fe^{2+}	1.28–1.29	3.51–3.53		(1),(3)
Andradite	$Ca_3(Al,Fe^{3+})_2(SiO_4)_3$	M	Fe^{3+}	0.40–0.41	0.5–0.6		(1),(3)
Epidote	$Ca_2(Fe^{3+},Al)_3O(OH)(Si_2O_7)(SiO_4)$	M3	Fe^{3+}	0.34–0.36	1.9–2.1		(3)
Px ferrosilite	$Fe_2Si_2O_6$	M1	Fe^{2+}	1.17–1.18	2.48–2.49		(1),(3)
		M2	Fe^{2+}	1.13	1.91–1.93		(1),(3)
Px ferrosi-ensta	$(Mg,Fe^{2+},Mn)_2Si_2O_6$	M1	Fe^{2+}	1.15–1.18	2.35–2.69		(3)
		M2	Fe^{2+}	1.12–1.16	1.91–2.13		(3)
Px hedenbergite	$CaFe^{2+}Si_2O_6$	M1	Fe^{2+}	1.18–1.19	2.20–2.21		(1),(3)
		M1	Fe^{3+}	0.34	0.68		(1),(3)
Px diopside		M1	Fe^{2+}	1.16	1.87		(1)
		M2	Fe^{2+}	1.15	2.14		(1)
Px heden-diop	$Ca(Mg,Fe^{2+})Si_2O_6$	M1	Fe^{2+}	1.19	1.85–2.30		(3)
Px Aegirine	$(Na,Li)Fe^{3+}Si_2O_6$	M1	Fe^{3+}	0.39	0.30		(3)
Amph Trem-a		M1	Fe^{2+}	1.11	2.85		(1)
		M2	Fe^{2+}	1.12	1.80		(1)
		M3	Fe^{2+}	1.11	2.40		(1)
Amph Grunerite	$Fe_7Si_8O_{22}(OH)_2$	M1	Fe^{2+}	1.16	2.82		(3)
		M4	Fe^{2+}	1.10	1.8		(3)
Amph Cummingtonite-grunerite	$(Mg,Fe^{2+},Mn)_7Si_8O_{22}(OH)_2$	M1-M3	Fe^{2+}	1.16	2.82		(3)
		M4	Fe^{2+}	1.10	1.5–1.8		(3)
Amph Riebeckite	$Na(Fe^{2+})_3(Fe^{3+})_2Si_8O_{22}(OH)_2$	M1	Fe^{2+}	1.14	2.83		(3)
		M3	Fe^{2+}	1.11	2.32		(3)
		M2	Fe^{3+}	0.38	0.43		(3)
Amph Ferroactinolite	$Ca_2Fe_5Si_8O_{22}(OH)_2$	M1,M3	Fe^{2+}	1.15	2.81		(3)
		M2	Fe^{2+}	1.14	1.85–2.1		(3)
		M4	Fe^{2+}	1.10	<1.8		(3)
Chlorite		T	Fe^{3+}	0.25	0.50		(1)
		M	Fe^{2+}	1.09	2.59		(1)
		M1	Fe^{2+}	1.11–1.12	2.3–2.4		(1)
		M2	Fe^{2+}	1.12–1.14	2.66–2.68		(1)
		T	Fe^{3+}	0.12	0.39		(1)
		M	Fe^{3+}	0.35	0.4		(1)
		M	Fe^{3+}	0.35	0.65		(1)
Bi-Phlogopite		M	Fe^{2+}	1.13	2.57		(1)
		M	Fe^{2+}	1.12	2.15		(1)
		M	Fe^{3+}	0.40	0.87		(1)
		T	Fe^{3+}	0.20	0.75		(1)
Fe-Biotite		M1	Fe^{2+}	1.01–1.15	2.10–2.22		(2),(3)
		M2	Fe^{2+}	1.05–1.14	2.56–2.63		(2),(3)
		M1	Fe^{3+}	0.39–0.50	0.72–0.88, 1.16–1.24		(2),(3)
		M2	Fe^{3+}	0.39–0.54	0.34–0.66		(2),(3)
Fe-Talc	$Fe_xMg_{3-x}Si_4O_{10}(OH)_2$	M2	Fe^{2+}	1.13	2.57–2.6		(1),(3)
		M	Fe^{2+}	1.12	2.15		(1)
Minnesotaite	$Fe_3Si_4O_{10}(OH)_2$	M	Fe^{2+}	1.13	2.72–2.75		(10)
Stilpnomelane	$K(Fe^{2+},Mg,Fe^{3+})_8(Si,Al)_{12}(O,OH)_{27}\cdot nH2O$	M1	Fe^{2+}	1.13	2.27		(9)
		M2	Fe^{2+}	1.16	2.66		(9)
		M1,M2,M4	Fe^{3+}	0.41	1.18		(9)
		M3	Fe^{3+}	0.36	2.07		(9)
Glauconite		M	Fe^{2+}	1.11	2.71		(1)
		M	Fe^{3+}	0.33	0.45		(1)
		M	Fe^{3+}	0.34	0.99		(1)
Lizardite		M	Fe^{2+}	1.14	2.70		(1)
		M	Fe^{3+}	0.40	0.70		(1)
		T	Fe^{3+}	0.24	0.39		(1)
Chrysotile		M	Fe^{2+}	1.13	2.75		(1)
		M	Fe^{3+}	0.31	0.86		(1)
		T	Fe^{3+}	0.18	0.33		(1)
Hematite	α-Fe_2O_3		Fe^{3+}	0.36	−0.19	51.7	(3)
				0.38	−0.24	51.5	(8)
Ilmenite	$Fe_{1+x}Ti_{1-x}O_3$		Fe^{2+}	1.0–1.1	0.65–0.70		(3)
			Fe^{3+}	0.3	0.3–0.5		(3)
Pure magnetite	α-Fe_3O_4	T	Fe^{3+}	0.28		49.0	(3)
				0.25		48.9	(7)
		M	$Fe^{2.5+}$	0.66		45.9	(3)
				0.65		45.7	(7)

(*continued on next page*)

Table A2 (*continued*)

Mineral		Contrib*	Fe valency	δ (mm/s)	QS/ΔEQ (mm/s)	B_{Hf} (T)	Reference
Oxidized magnetite	$Fe_{3-x}O_4$	T	Fe^{3+}	0.39	0.11	50.3	(8)
		M	$Fe^{2+/3+}$	0.78	0.28	46.5	(8)
Pure maghemite	γ- Fe_2O_3	T	Fe^{3+}	0.24		49.9	(3)
		M	Fe^{3+}	0.36		49.9	
Goethite	γ-FeO(OH)		Fe^{3+}	0.37	−0.28	38.1	(3)
				0.38	0.60		(8)
Pyrite	FeS_2		Fe^{2+}	0.31	0.61		(3)
				0.22–0.24	0.59–0.62		(4)
Triolite	FeS		Fe^{2+}	0.7–0.9	−0.3	30–32	(3)
Siderite	$FeCO_3$		Fe^{2+}	1.2	1.79		(3)
				1.23–1.27	1.77–1.83		(5)
Ankerite	$Ca_xFe_{2-x}(CO_3)_2$		Fe^{2+}	1.2	1.44–1.48		(3)
				1.20–1.23	1.50–1.60		(4)
Greenalite	$Fe_3^{2+}Si_2O_5(OH)_4$		Fe^{2+}	1.15	2.75		(3)
Spinel	$(Mg_{1-x}Fe_x^{2+})(Al_{2-y}Fe_y^{3+})O_4$	M	Fe^{3+}	0.31–0.34	0.64–0.78		(6)
		M	Fe^{2+}	1.03–1.10	1.54–1.69		(6)
		T	Fe^{2+}	0.90–0.91	0.83–0.92		(6)
		T	Fe^{2+}	0.73–0.85	1.50–1.81		(6)

Appendix A5. S2 sample characterization through optical microscopy, XRD and SEM for Pre-Mössbauer processing

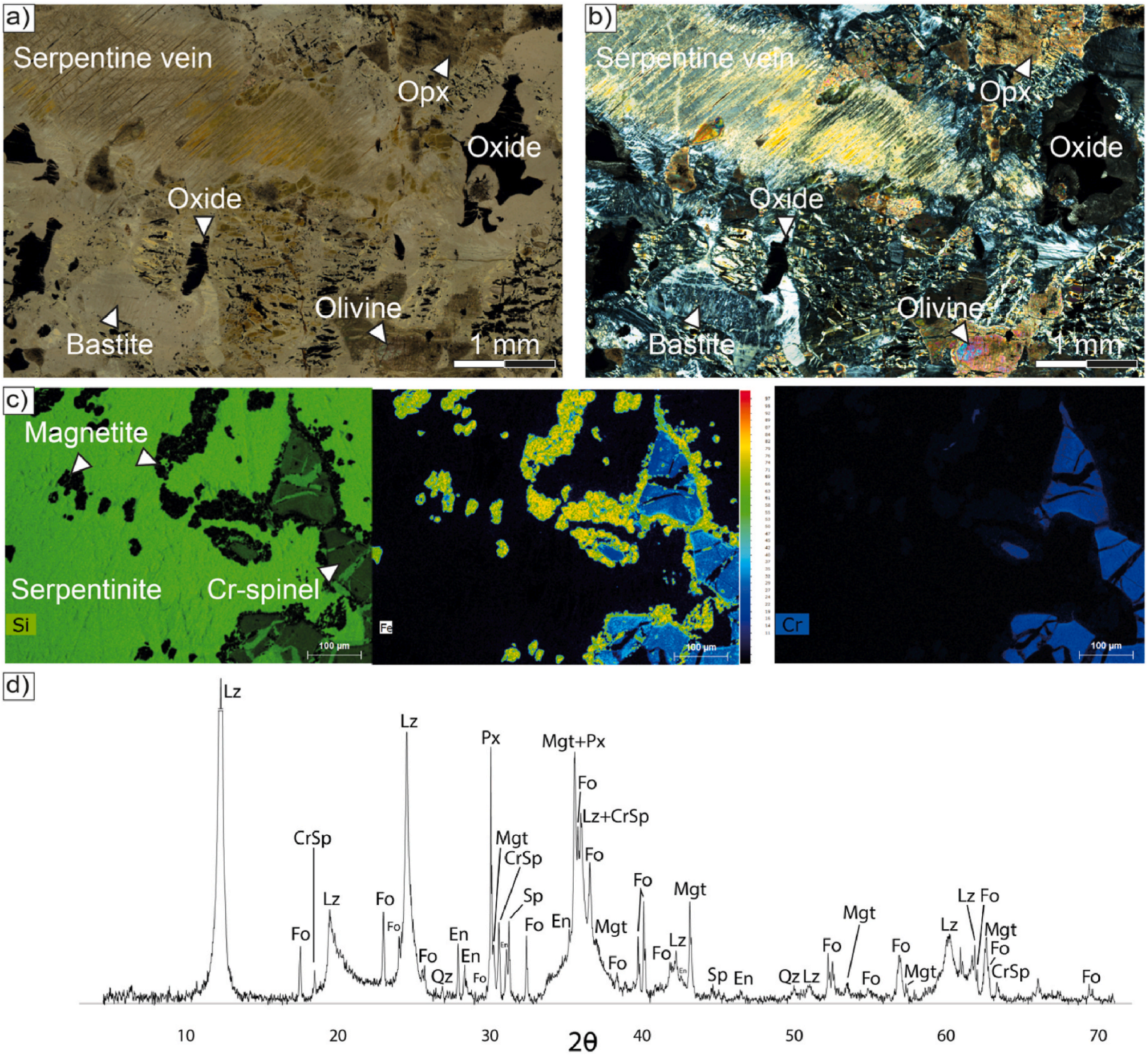

Fig. A3. Pre-Mössbauer sample characterization, performed on S2. (a,b) Photomicrograph of the thin section observed in Polar-plane light. (c) Elementary mapping highlighting the distribution of Si, Fe and Cr in the sample. (d) XRD pattern and peak indexing of the bulk sample powder. Lz refers to lizardite, Mgt to magnetite, Fo to forsterite, CrSp to Cr-spinel, Px to pyroxene, En to enstatite. In this sample, Fe is carried by magnetite, forsterite, lizardite, pyroxene such as enstatite, and Cr-Spinel.

Appendix A6. S3 sample characterization through optical microscopy, XRD and SEM for Pre-Mössbauer processing

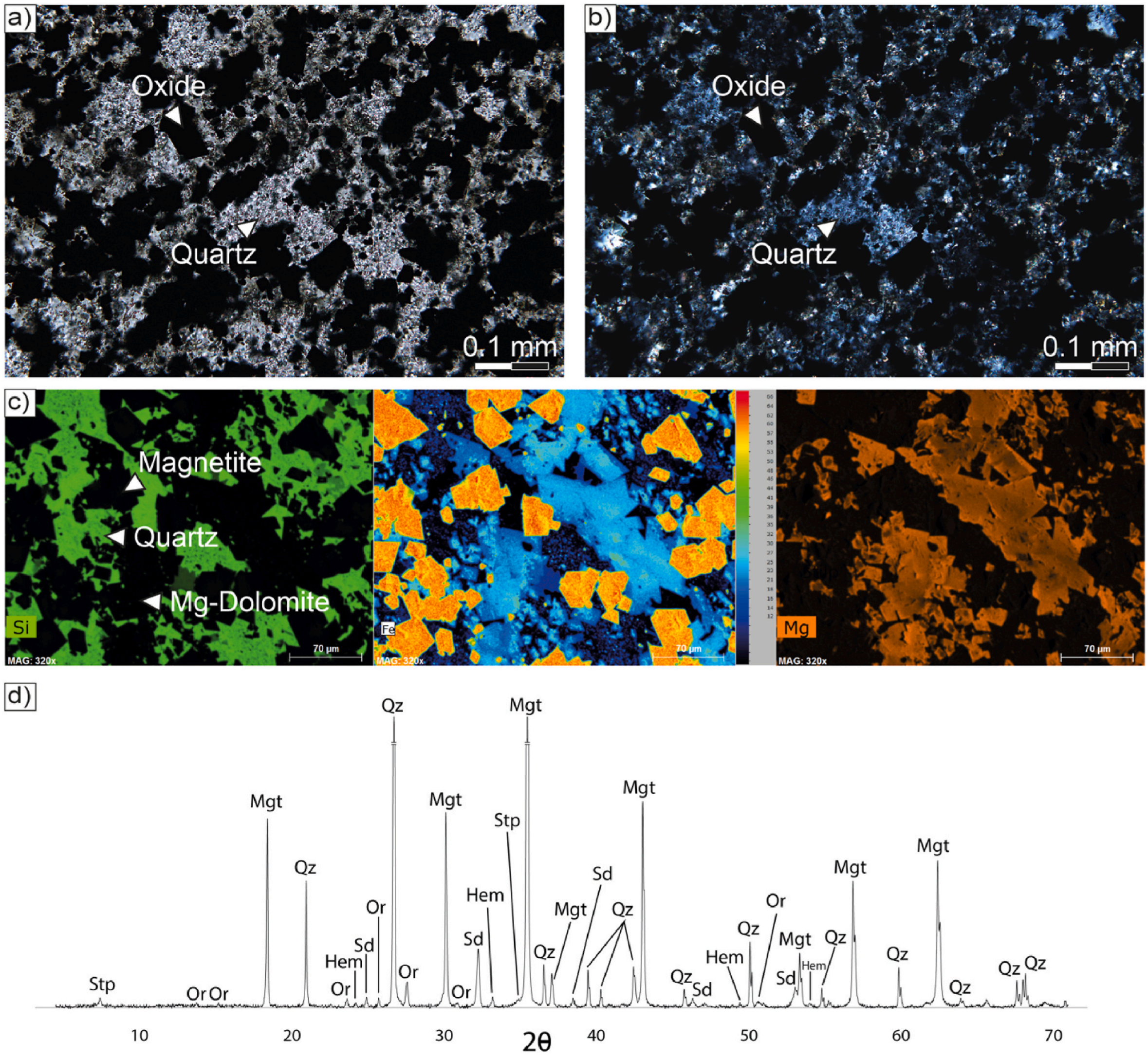

Fig. A4. Pre-Mössbauer sample characterization, performed on S3. (a,b) Photomicrograph of the thin section observed in Polar-plane light. (c) Elementary mapping highlighting the distribution of Si, Fe and Mg in the sample. (d) XRD pattern and peak indexing of the bulk sample powder. Stp refers to stilpnomelane, Mgt to magnetite, Qz to quartz, Ab to albite, An to anorthite, Sd to siderite, Hem to hematite. In this sample, Fe is carried by magnetite, siderite, and to some extent possibly by stilpnomelane.

Appendix A7. S4 sample characterization through optical microscopy, XRD and SEM for Pre-Mössbauer processing

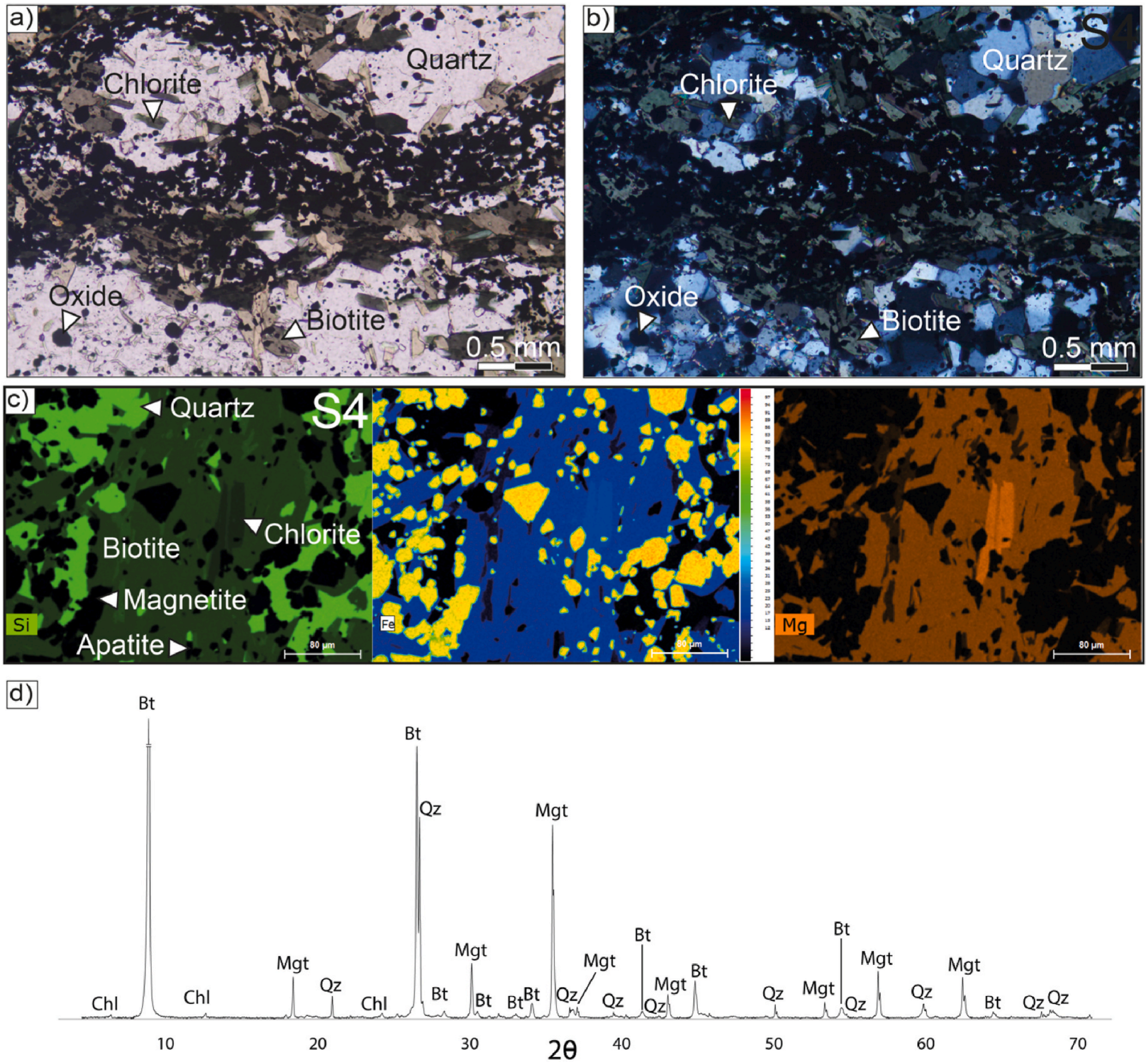

Fig. A5. Pre-Mössbauer sample characterization, performed on S4. (a,b) Photomicrograph of the thin section observed in Polar-plane light. (c) Elementary mapping highlighting the distribution of Si, Fe and Mg in the sample. (d) XRD pattern and peak indexing of the bulk sample powder. Chl refers to chlorite, Bt to biotite, Mgt to magnetite, Qz to quartz. In this sample, Fe is carried by magnetite, biotite, and to some extent possibly by chlorite.

Appendix A8. S5 sample characterization through optical microscopy, XRD and SEM for Pre-Mössbauer processing

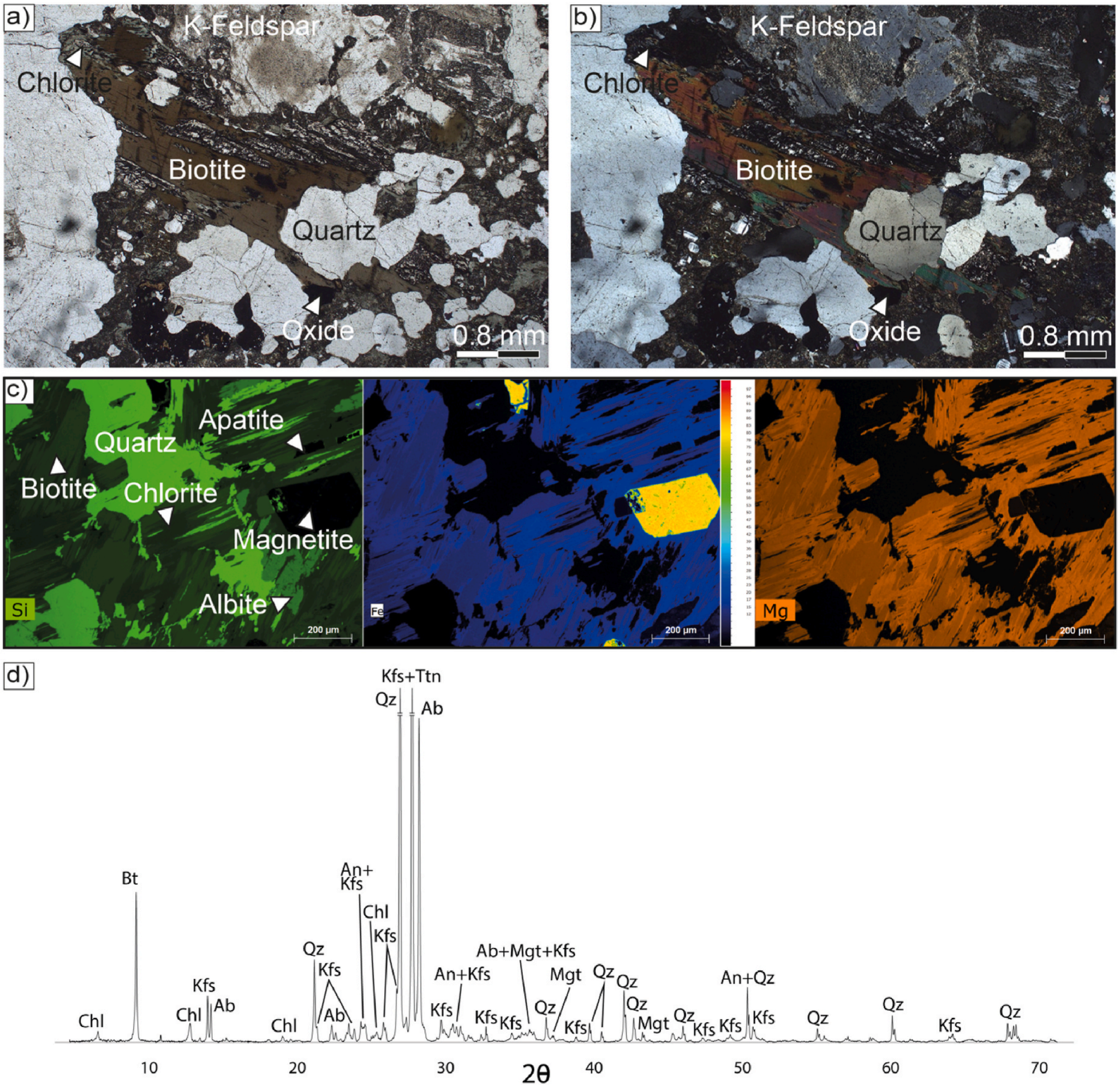

Fig. A6. Pre-Mössbauer sample characterization, performed on S5. (a,b) Photomicrograph of the thin section observed in Polar-plane light. (c) Elementary mapping highlighting the distribution of Si, Fe and Mg in the sample. (d) XRD pattern and peak indexing of the bulk sample powder. Chl refers to chlorite, Bt to biotite, Kfs to orthose, Ab to albite, An to anorthite, Qz to quartz, Ttn to titanite, Mgt to magnetite. In this sample, Fe is carried by biotite and to some extent possibly by chlorite, magnetite and titanite.

Appendix A9. Hyperfine parameters used to fit the Mössbauer spectra acquired on the samples (S1–S5) at low or room temperature (6K–295K) in source velocity of 12 mm/s or 4 mm/s (HV-LV). Relative areas (RA%) of each subspectrum contribution are also provided, as well as χ^2 to provide first order estimate of the relative reliability of the fitting

Table A3

Hyperfine parameters used to fit the Mössbauer spectra presented in Fig. 4 and associated $Fe^{2+}/\sum Fe$ ratios calculated for each sample. No error bar is provided in this table, which is discussed in details in section 4.4.

Sample	Contribution	Fe valency	δ (mm/s)	QS/ΔEQ (mm/s)	B_{Hf} (T)	RA (%)	χ^2	Bulk $Fe^{2+}/\sum Fe$
S1-6K-HV	Olivine M1	Fe^{2+}	1.18	2.94		29	0.62	0.88
	Olivine M2	Fe^{2+}	0.94	2.55		28		
	Orthopyroxene M1	Fe^{2+}	1.48	2.72		31		
	Cr-Spinel T	Fe^{3+}	0.38	0.83		12		
S1-295K-HV	Olivine M1	Fe^{2+}	1.15	3.11		20	2.00	0.89
	Olivine M2	Fe^{2+}	1.14	2.91		34		
	Orthopyroxene M1	Fe^{2+}	1.15	2.08		26		
	Orthopyroxene M2	Fe^{2+}	1.23	2.44		10		
	Cr-Spinel T	Fe^{3+}	0.38	0.83		11		

(continued on next page)

Table A3 (*continued*)

Sample	Contribution	Fe valency	δ (mm/s)	QS/ΔEQ (mm/s)	B_{Hf} (T)	RA (%)	χ^2	Bulk $Fe^{2+}/\sum Fe$
S1–295K-LV	Olivine M1	Fe^{2+}	1.16	3.09		24	0.18	0.88
	Olivine M2	Fe^{2+}	1.14	2.88		28		
	Orthopyroxene M1	Fe^{2+}	1.14	2.10		31		
	Orthopyroxene M2	Fe^{2+}	1.29	2.40		5		
	Cr-Spinel T	Fe^{3+}	0.38	0.83		12		
S2-6K-HV	Serpentine M1	Fe^{2+}	1.19	2.89		35	0.26	0.51
	Cr-Spinel T	Fe^{3+}	0.34	0.49		8		
	Magnetite M1	$Fe^{2.5+}$	0.74		50.96	14		
	Magnetite M2	$Fe^{2.5+}$	0.85		54.16	10		
	Magnetite M3	Fe^{2+}	1.24		35.44	8		
	Magnetite T	Fe^{3+}	0.19		52.51	25		
S2-295K-HV	Serpentine M1	Fe^{2+}	1.11	2.74		40	0.97	0.56
	Cr-Spinel T	Fe^{3+}	0.34	0.52		8		
	Magnetite M	$Fe^{2.5+}$	0.70		46.04	33		
	Magnetite T	Fe^{3+}	0.29		49.37	19		
S2–295K-LV	Serpentine M1	Fe^{2+}	1.14	2.77		33	1.21	0.50
	Cr-Spinel T	Fe^{3+}	0.36	0.56		12		
	Magnetite M	$Fe^{2.5+}$	0.74		46.89	35		
	Magnetite T	Fe^{3+}	0.28		51.75	20		
S3-6K-HV	Fe-carbonate	Fe^{2+}	0.96	1.55		3	0.58	0.35
	Magnetite M1	$Fe^{2.5+}$	0.73		51.47	41		
	Magnetite M2	$Fe^{2.5+}$	0.78		55.60	11		
	Magnetite M3	Fe^{2+}	1.10	2.03	34.87	8		
	Magnetite T	Fe^{3+}	0.19		52.06	35		
S3-295K-HV	Fe-carbonate	Fe^{2+}	1.20	1.76		13	1.56	0.40
	Magnetite M	$Fe^{2.5+}$	0.65		45.67	55		
	Magnetite T	Fe^{3+}	0.29		48.96	31		
S4-6K-HV	Biotite M2 (?)	Fe^{2+}	1.15	3.00		11	2.47	0.37
	Biotite M1 (?)	Fe^{3+}	0.43	0.61		5		
	Magnetite M1	$Fe^{2.5+}$	0.73		52.85	37		
	Magnetite M2	$Fe^{2.5+}$	0.30		46.90	6		
	Magnetite M3	Fe^{2+}	1.32		36.00	11		
	Magnetite T	Fe^{3+}	0.3		52.56	0.32		
S4-295K-HV	Biotite M2	Fe^{2+}	1.12	2.60		0.17	1.44	0.42
	Biotite M1	Fe^{3+}	0.37	0.76		0.07		
	Magnetite M	$Fe^{2.5+}$	0.66		45.67	0.49		
	Magnetite T	Fe^{3+}	0.28		48.89	0.27		
S5-6K-HV	Biotite M2 (?)	Fe^{2+}	1.22	2.70		0.23	0.38	0.47
	Biotite M1 (?)	Fe^{3+}	0.33	1.01		0.10		
	Magnetite M1	$Fe^{2.5+}$	0.40		52.31	0.38		
	Magnetite M2	$Fe^{2.5+}$	0.93		43.28	0.04		
	Magnetite M3	Fe^{2+}	1.35		28.49	0.07		
	Magnetite T	Fe^{3+}	1.00		52.41	0.19		
S5-295K-HV	Biotite M1	Fe^{2+}	1.09	2.29		0.14	0.77	0.46
	Biotite M2	Fe^{2+}	1.13	2.64		0.16		
	Biotite M1	Fe^{3+}	0.42	0.95		0.15		
	Magnetite M	$Fe^{2.5+}$	0.34		45.89	0.31		
	Magnetite T	Fe^{3+}	0.30		49.36	0.24		

Data availability

Data will be made available on request.

References

Anastácio, A.S., Harris, B., Yoo, H.-I., Fabris, J.D., Stucki, J.W., 2008. Limitations of the ferrozine method for quantitative assay of mineral systems for ferrous and total iron. Geochem. Cosmochim. Acta 72, 5001–5008. https://doi.org/10.1016/j.gca.2008.07.009.

Andreani, M., Daniel, I., Pollet-Villard, M., 2013a. Aluminum speeds up the hydrothermal alteration of olivine. Am. Mineral. 98, 1738–1744. https://doi.org/10.2138/am.2013.4469.

Andreani, M., Muñoz, M., Marcaillou, C., Delacour, A., 2013b. µXANES study of iron redox state in serpentine during oceanic serpentinization. Lithos 178, 70–83. https://doi.org/10.1016/j.lithos.2013.04.008.

Barbier, S., Huang, F., Andreani, M., Tao, R., Hao, J., Eleish, A., Prabhu, A., Minhas, O., Fontaine, K., Fox, P., Daniel, I., 2020. A review of H2, CH4, and hydrocarbon formation in experimental serpentinization using network analysis. Front. Earth Sci. 8, 209. https://doi.org/10.3389/feart.2020.00209.

Barnes, I., O'Neil, J.R., Trescases, J.J., 1978. Present day serpentinization in New Caledonia, Oman and Yugoslavia. Geochem. Cosmochim. Acta 42, 144–145. https://doi.org/10.1016/0016-7037(78)90225-9.

Boreham, C.J., Edwards, D.S., Czado, K., Rollet, N., Wang, L., van der Wielen, S., Champion, D., Blewett, R., Feitz, A., Henson, P.A., 2021. Hydrogen in Australian natural gas: occurrences, sources and resources. The APPEA Journal 61, 163. https://doi.org/10.1071/AJ20044.

Carlin, W., Malvoisin, B., Brunet, F., Lanson, B., Findling, N., Lanson, M., Fargetton, T., Jeannin, L., Lhote, O., 2024. Kinetics of low-temperature H2 production in ultramafic rocks by ferroan brucite oxidation. Geochem. Persp. Let. 29, 27–32. https://doi.org/10.7185/geochemlet.2408.

Chen, C., Dong, Y., Thompson, A., 2023. Electron transfer, atom exchange, and transformation of iron minerals in soils: the influence of soil organic matter. Environ. Sci. Technol. 57, 10696–10707. https://doi.org/10.1021/acs.est.3c01876.

Clerc, C., Lagabrielle, Y., Neumaier, M., Reynaud, J.-Y., De Saint Blanquat, M., 2012. Exhumation of subcontinental mantle rocks: evidence from ultramafic-bearing clastic deposits nearby the Lherz peridotite body, French Pyrenees. Bull. Soc. Geol. Fr. 183, 443–459. https://doi.org/10.2113/gssgfbull.183.5.443.

Combaudon, V., Sissmann, O., Bernard, S., Viennet, J.-C., Megevand, V., Le Guillou, C., Guélard, J., Martinez, I., Guyot, F., Derluyn, H., Deville, E., 2024. Are the Fe-rich-clay veins in the igneous rock of the Kansas (USA) Precambrian crust of magmatic origin? Lithos 474–475, 107583. https://doi.org/10.1016/j.lithos.2024.107583.

Contreras Acosta, I.C., Khodadadzadeh, M., Gloaguen, R., 2021. Resolution enhancement for drill-core hyperspectral mineral mapping. Remote Sens. 13, 2296. https://doi.org/10.3390/rs13122296.

Corre, B., Lagabrielle, Y., Labaume, P., Fourcade, S., Clerc, C., Ballèvre, M., 2016. Deformation associated with mantle exhumation in a distal, hot passive margin environment: new constraints from the Saraillé Massif (Chaînons Béarnais, North-Pyrenean Zone). Comptes Rendus. Geoscience 348, 279–289. https://doi.org/10.1016/j.crte.2015.11.007.

Cotten, J., Le Dez, A., Bau, M., Caroff, M., Maury, R.C., Dulski, P., Fourcade, S., Bohn, M., Brousse, R., 1995. Origin of anomalous rare-earth element and yttrium enrichments in subaerially exposed basalts: evidence from French Polynesia. Chem. Geol. 119, 115–138. https://doi.org/10.1016/0009-2541(94)00102-E.

Daniels, J.M., Rosencwaig, A., 1969. Mössbauer spectroscopy of stoichiometric and non-stoichiometric magnetite. J. Phys. Chem. Solid. 30, 1561–1571. https://doi.org/10.1016/0022-3697(69)90217-0.

De Grave, E., Vochten, R., 1985. An57Fe mössbauer effect study of ankerite. Phys. Chem. Miner. 12, 108–113. https://doi.org/10.1007/BF01046835.

Doriguetto, A.C., Fernandes, N.G., Persiano, A.I.C., Filho, E.N., Grenèche, J.M., Fabris, J. D., 2003. Characterization of a natural magnetite. Phys. Chem. Miner. 30, 249–255. https://doi.org/10.1007/s00269-003-0310-x.

Dyar, M.D., 2002. Optical and mossbauer spectroscopy of iron in micas. Rev. Mineral. Geochem. 46, 313–349. https://doi.org/10.2138/rmg.2002.46.06.

Dyar, M.D., Agresti, D.G., Schaefer, M.W., Grant, C.A., Sklute, E.C., 2006. Mössbauer spectroscopy of Earth and Planetary materials. Annu. Rev. Earth Planet Sci. 34, 83–125. https://doi.org/10.1146/annurev.earth.34.031405.125049.

Ellison, E.T., Templeton, A.S., Zeigler, S.D., Mayhew, L.E., Kelemen, P.B., Matter, J.M., The Oman Drilling Project Science Party, 2021. Low-temperature hydrogen formation during aqueous alteration of serpentinized peridotite in the samail ophiolite. JGR Solid Earth 126, e2021JB021981. https://doi.org/10.1029/2021JB021981.

Fehse, M., Iadecola, A., Sougrati, M.T., Conti, P., Giorgetti, M., Stievano, L., 2019. Applying chemometrics to study battery materials: towards the comprehensive analysis of complex operando datasets. Energy Storage Mater. 18, 328–337. https://doi.org/10.1016/j.ensm.2019.02.002.

Forshaw, J.B., Pattison, D.R.M., 2021. Ferrous/ferric (Fe2+/Fe3+) partitioning among silicates in metapelites. Contrib. Mineral. Petrol. 176, 63. https://doi.org/10.1007/s00410-021-01814-4.

Frimmel, H., 1998. Neoproterozoic tectono-thermal evolution of the Gariep Belt and its basement, Namibia and South Africa. Precambr. Res. 90, 1–28. https://doi.org/10.1016/S0301-9268(98)00029-1.

Frimmel, H.E., 2011. Chapter 17 the kaigas and numees formations, port nolloth group, in South Africa and Namibia. Memoirs 36, 223–231. https://doi.org/10.1144/M36.17.

Fuchs, Y., Linares, J., Mellini, M., 1998. Mössbauer and infrared spectrometry of lizardite- 1T from Monte Fico, Elba. Phys. Chem. Miner. 26, 111–115. https://doi.org/10.1007/s002690050167.

Fukuyama, D., Shinoda, K., Takagi, D., Kobayashi, Y., 2022. Compositional dependence of intensity and electric field gradient tensors for Fe^{2+} at the *M*1 site in Ca–rich pyroxene by single crystal Mössbauer spectroscopy. J. Mineral. Petrol. Sci. 117, n/a. https://doi.org/10.2465/jmps.220506.

García, J., Subías, G., 2004. The Verwey transition—a new perspective. J. Phys. Condens. Matter 16, R145–R178. https://doi.org/10.1088/0953-8984/16/7/R01.

Geymond, U., Briolet, T., Combaudon, V., Sissmann, O., Martinez, I., Duttine, M., Moretti, I., 2023. Reassessing the role of magnetite during natural hydrogen generation. Front. Earth Sci. 11, 1169356. https://doi.org/10.3389/feart.2023.1169356.

Geymond, U., Ramanaidou, E., Lévy, D., Ouaya, A., Moretti, I., 2022. Can weathering of banded iron formations generate natural hydrogen? Evidence from Australia, Brazil and South Africa. Minerals 12, 163. https://doi.org/10.3390/min12020163.

Gorski, C.A., Handler, R.M., Beard, B.L., Pasakarnis, T., Johnson, C.M., Scherer, M.M., 2012. Fe atom exchange between aqueous Fe $^{2+}$ and magnetite. Environ. Sci. Technol. 46, 12399–12407. https://doi.org/10.1021/es204649a.

Gorski, C.A., Scherer, M.M., 2010. Determination of nanoparticulate magnetite stoichiometry by Mossbauer spectroscopy, acidic dissolution, and powder X-ray diffraction: a critical review. Am. Mineral. 95, 1017–1026. https://doi.org/10.2138/am.2010.3435.

Gorski, C.A., Scherer, M.M., 2009. Influence of magnetite stoichiometry on Fe ^{II} uptake and nitrobenzene reduction. Environ. Sci. Technol. 43, 3675–3680. https://doi.org/10.1021/es803613a.

Grandjean, F., Long, G.J., 2021. Best practices and protocols in mössbauer spectroscopy. Chem. Mater. 33, 3878–3904. https://doi.org/10.1021/acs.chemmater.1c00326.

Hepburn, L.E., Butler, I.B., Boyce, A., Schröder, C., 2020. The use of operationally-defined sequential Fe extraction methods for mineralogical applications: a cautionary tale from Mössbauer spectroscopy. Chem. Geol. 543, 119584. https://doi.org/10.1016/j.chemgeo.2020.119584.

Husler, J., Ferriss, E.D.A., Helean, K.B., Bryan, C.R., Brady, P.V., 2011. Optimised ferrozine micro-method for the determination of ferrous and ferric iron in rocks and minerals. Geostand. Geoanal. Res. 35, 39–44. https://doi.org/10.1111/j.1751-908X.2010.00041.x.

Inoue, A., Inoué, S., Utada, M., 2018. Application of chlorite thermometry to estimation of formation temperature and redox conditions. Clay Miner. 53, 143–158. https://doi.org/10.1180/clm.2018.10.

Jen, L.-S., 1973. The determination of iron(II) in silicate rocks and minerals. Anal. Chim. Acta 66, 315–318. https://doi.org/10.1016/S0003-2670(01)82546-0.

Joos, A., Rümenapp, C., Wagner, F.E., Gleich, B., 2016. Characterisation of iron oxide nanoparticles by Mössbauer spectroscopy at ambient temperature. J. Magn. Magn Mater. 399, 123–129. https://doi.org/10.1016/j.jmmm.2015.09.060.

Klein, F., Bach, W., McCollom, T.M., 2013. Compositional controls on hydrogen generation during serpentinization of ultramafic rocks. Lithos 178, 55–69. https://doi.org/10.1016/j.lithos.2013.03.008.

Klingelhöfer, G., Morris, R.V., Bernhardt, B., Rodionov, D., De Souza, P.A., Squyres, S.W., Foh, J., Kankeleit, E., Bonnes, U., Gellert, R., Schröder, C., Linkin, S., Evlanov, E., Zubkov, B., Prilutski, O., 2003. Athena MIMOS II Mössbauer spectrometer investigation. J. Geophys. Res. 108, 2003JE002138. https://doi.org/10.1029/2003JE002138.

Lagabrielle, Y., Asti, R., Fourcade, S., Corre, B., Labaume, P., Uzel, J., Clerc, C., Lafay, R., Picazo, S., 2019. Mantle exhumation at magma-poor passive continental margins. Part II: tectonic and metasomatic evolution of large-displacement detachment faults preserved in a fossil distal margin domain (Saraillé lherzolites, northwestern Pyrenees, France). BSGF - Earth Sci. Bull. 190, 14. https://doi.org/10.1051/bsgf/2019013.

Lagabrielle, Y., Bodinier, J.-L., 2008. Submarine reworking of exhumed subcontinental mantle rocks: field evidence from the Lherz peridotites, French Pyrenees. Terra Nova 20, 11–21. https://doi.org/10.1111/j.1365-3121.2007.00781.x.

Lagabrielle, Y., Labaume, P., De Saint Blanquat, M., 2010. Mantle exhumation, crustal denudation, and gravity tectonics during Cretaceous rifting in the Pyrenean realm (SW Europe): insights from the geological setting of the lherzolite bodies: Pyrenean Lherzolites, Gravity Tectonics. Tectonics 29. https://doi.org/10.1029/2009TC002588.

Latta, D.E., Gorski, C.A., Boyanov, M.I., O'Loughlin, E.J., Kemner, K.M., Scherer, M.M., 2012. Influence of magnetite stoichiometry on U^{VI} reduction. Environ. Sci. Technol. 46, 778–786. https://doi.org/10.1021/es2024912.

Le Roux, V., Bodinier, J.-L., Tommasi, A., Alard, O., Dautria, J.-M., Vauchez, A., Riches, A.J.V., 2007. The Lherz spinel lherzolite: refertilized rather than pristine mantle. Earth Planet Sci. Lett. 259, 599–612. https://doi.org/10.1016/j.epsl.2007.05.026.

Lefeuvre, N., Truche, L., Donzé, F., Ducoux, M., Barré, G., Fakoury, R., Calassou, S., Gaucher, E.C., 2021. Native H $_2$ exploration in the western pyrenean foothills. Geochem Geophys Geosyst 22. https://doi.org/10.1029/2021GC009917.

Lévy, D., Roche, V., Pasquet, G., Combaudon, V., Geymond, U., Loiseau, K., Moretti, I., 2023. Natural H $_2$ exploration: tools and workflows to characterize a play. Sci. Tech. Energ. Transition 78, 27. https://doi.org/10.2516/stet/2023021.

Lodya, J.A., Pollak, H., Nell, J., Albers, A., 1994. Mössbauer spectroscopy and magnetic susceptibility studies of natural chromites. Hyperfine Interact. 93, 1789–1794. https://doi.org/10.1007/BF02072947.

Loiseau, K., Aubourg, C., Petit, V., Bordes, S., Lefeuvre, N., Thomas, E., Hoareau, G., Moretti, I., 2024. Hydrogen generation and heterogeneity of the serpentinization process at all scales: Turon de Técouère lherzolite case study, Pyrenees (France). Geoenergy 2. https://doi.org/10.1144/geoenergy2023-024 geoenergy2023-024.

Maffione, M., Morris, A., Plümper, O., Van Hinsbergen, D.J.J., 2014. Magnetic properties of variably serpentinized peridotites and their implication for the evolution of oceanic core complexes. Geochem. Geophys. Geosyst. 15, 923–944. https://doi.org/10.1002/2013GC004993.

Malczewski, D., Popiel, E., 2008. ^{57}Fe Mössbauer study of the oxidation state of iron in stilpnomelane from granite pegmatites in Poland. Am. Mineral. 93 (8–9), 1404–1411. https://doi.org/10.2138/am.2008.2719.

Malvoisin, B., Brunet, F., Carlut, J., Rouméjon, S., Cannat, M., 2012. Serpentinization of oceanic peridotites: 2. Kinetics and processes of San Carlos olivine hydrothermal alteration: kinetics of serpentinization. J. Geophys. Res. 117. https://doi.org/10.1029/2011JB008842 n/a-n/a.

Mayhew, L.E., Ellison, E.T., McCollom, T.M., Trainor, T.P., Templeton, A.S., 2013. Hydrogen generation from low-temperature water–rock reactions. Nat. Geosci. 6, 478–484. https://doi.org/10.1038/ngeo1825.

McCammon, C., 2021. Mössbauer spectroscopy with high spatial resolution: spotlight on geoscience. In: Yoshida, Y., Langouche, G. (Eds.), Modern Mössbauer Spectroscopy, Topics in Applied Physics. Springer Singapore, Singapore, pp. 221–266. https://doi.org/10.1007/978-981-15-9422-9_5.

McCollom, T.M., Klein, F., Robbins, M., Moskowitz, B., Berquó, T.S., Jöns, N., Bach, W., Templeton, A., 2016. Temperature trends for reaction rates, hydrogen generation, and partitioning of iron during experimental serpentinization of olivine. Geochem. Cosmochim. Acta 181, 175–200. https://doi.org/10.1016/j.gca.2016.03.002.

McGuire, A.V., Dyar, M.D., Nielson, J.E., 1991. Metasomatic oxidation of upper mantle periodotite. Contrib. Mineral. Petrol. 109, 252–264. https://doi.org/10.1007/BF00306483.

Moretti, I., Geymond, U., Pasquet, G., Aimar, L., Rabaute, A., 2022. Natural hydrogen emanations in Namibia: field acquisition and vegetation indexes from multispectral satellite image analysis. Int. J. Hydrogen Energy S0360319922036631. https://doi.org/10.1016/j.ijhydene.2022.08.135.

Murad, E., 2010. Mössbauer spectroscopy of clays, soils and their mineral constituents. Clay Miner. 45, 413–430. https://doi.org/10.1180/claymin.2010.045.4.413.

Murray, J., Clément, A., Fritz, B., Schmittbuhl, J., Bordmann, V., Fleury, J.M., 2020. Abiotic hydrogen generation from biotite-rich granite: a case study of the Soultz-sous-Forêts geothermal site, France. Appl. Geochem. 119, 104631. https://doi.org/10.1016/j.apgeochem.2020.104631.

Neal, C., Stanger, G., 1983. Hydrogen generation from mantle source rocks in Oman. Earth Planet Sci. Lett. 66, 315–320. https://doi.org/10.1016/0012-821X(83)90144-9.

Neubeck, A., Duc, N.T., Bastviken, D., Crill, P., Holm, N.G., 2011. Formation of H2 and CH4by weathering of olivine at temperatures between 30 and 70°C. Geochem. Trans. 12, 6. https://doi.org/10.1186/1467-4866-12-6.

Notini, L., Schulz, K., Kubeneck, L.J., Grigg, A.R.C., Rothwell, K.A., Fantappiè, G., ThomasArrigo, L.K., Kretzschmar, R., 2023. A new approach for investigating iron mineral transformations in soils and sediments using^{57} Fe-labeled minerals and^{57} Fe mössbauer spectroscopy. Environ. Sci. Technol. 57, 10008–10018. https://doi.org/10.1021/acs.est.3c00434.

Osselin, F., Soulaine, C., Fauguerolles, C., Gaucher, E.C., Scaillet, B., Pichavant, M., 2022. Orange hydrogen is the new green. Nat. Geosci. 15, 765–769. https://doi.org/10.1038/s41561-022-01043-9.

Pasquet, G., Houssein Hassan, R., Sissmann, O., Varet, J., Moretti, I., 2021. An attempt to study natural H2 resources across an oceanic ridge penetrating a continent: the asal–ghoubbet rift (republic of Djibouti). Geosciences 12, 16. https://doi.org/10.3390/geosciences12010016.

Rancourt, D.G., 1994. Mössbauer spectroscopy of minerals: I. Inadequacy of Lorentzian-line doublets in fitting spectra arising from quadrupole splitting distributions. Phys. Chem. Miner. 21, 244–249. https://doi.org/10.1007/BF00202138.

Rasmussen, B., Fletcher, I.R., Muhling, J.R., 2007. In situ U–Pb dating and element mapping of three generations of monazite: unravelling cryptic tectonothermal events in low-grade terranes. Geochem. Cosmochim. Acta 71, 670–690. https://doi.org/10.1016/j.gca.2006.10.020.

Reid, A.J., Tiddy, C., Jagodzinski, E.A., Crowley, J.L., Conor, C., Brotodewo, A., Wade, C., 2021. Precise zircon U-Pb geochronology of Hiltaba Suite granites. Point Riley, Yorke Peninsula.

Řezníček, R., Chlan, V., Štěpánková, H., Novák, P., Żukrowski, J., Kozłowski, A., Kąkol, Z., Tarnawski, Z., Honig, J.M., 2017. Understanding the Mössbauer spectrum of magnetite below the Verwey transition: *Ab initio* calculations, simulation, and experiment. Phys. Rev. B 96, 195124. https://doi.org/10.1103/PhysRevB.96.195124.

Roche, V., Geymond, U., Boka-Mene, M., Delcourt, N., Portier, E., Revillon, S., Moretti, I., 2024. A new continental hydrogen play in Damara Belt (Namibia). Sci. Rep. 14, 11655. https://doi.org/10.1038/s41598-024-62538-6.

Sawatzky, G.A., Van Der Woude, F., Morrish, A.H., 1969. Mössbauer study of several ferrimagnetic spinels. Phys. Rev. 187, 747–757. https://doi.org/10.1103/PhysRev.187.747.

Schodlok, M.C., Whitbourn, L., Mason, J., Green, P., Berman, A., Jolivet, M., Martinez, R., 2016. HyLogger-3, a visible to shortwave and thermal infrared reflectance spectrometer system for drill core logging: functional description. Aust. J. Earth Sci. 63, 929–940. https://doi.org/10.1080/08120099.2016.1231133.

Seyfried, W.E., Foustoukos, D.I., Fu, Q., 2007. Redox evolution and mass transfer during serpentinization: an experimental and theoretical study at 200°C, 500bar with implications for ultramafic-hosted hydrothermal systems at Mid-Ocean Ridges. Geochem. Cosmochim. Acta 71, 3872–3886. https://doi.org/10.1016/j.gca.2007.05.015.

Sherwood Lollar, B., Onstott, T.C., Lacrampe-Couloume, G., Ballentine, C.J., 2014. The contribution of the Precambrian continental lithosphere to global H2 production. Nature 516, 379–382. https://doi.org/10.1038/nature14017.

Sissmann, O., Daval, D., Brunet, F., Guyot, F., Verlaguet, A., Pinquier, Y., Findling, N., Martinez, I., 2013. The deleterious effect of secondary phases on olivine carbonation yield: insight from time-resolved aqueous-fluid sampling and FIB-TEM characterization. Chem. Geol. 357, 186–202. https://doi.org/10.1016/j.chemgeo.2013.08.031.

Sommerfeld, M., Friedrich, B., 2022. Proposition of a thermogravimetric method to measure the ferrous iron content in metallurgical-grade chromite. Minerals 12, 109. https://doi.org/10.3390/min12020109.

Sougrati, M.T., Goellner, V., Schuppert, A.K., Stievano, L., Jaouen, F., 2016. Probing active sites in iron-based catalysts for oxygen electro-reduction: a temperature-dependent 57 Fe Mössbauer spectroscopy study. Catal. Today 262, 110–120. https://doi.org/10.1016/j.cattod.2015.10.017.

Sougrati, M.T., Jouen, S., Hannoyer, B., Lefez, B., 2008. Hyperfine interactions and lattice dynamics of Sn21O6Cl16(OH)14. J. Solid State Chem. 181, 2473–2479. https://doi.org/10.1016/j.jssc.2008.06.020.

Stevens, J.G., Khasanov, A., Miller, J.W., Pollak, H., Li, Z., 2005. M{\"o}ssbauer Mineral Handbook.

Syverson, D.D., Tutolo, B.M., Borrok, D.M., Seyfried, W.E., 2017. Serpentinization of olivine at 300 °C and 500 bars: an experimental study examining the role of silica on the reaction path and oxidation state of iron. Chem. Geol. 475, 122–134. https://doi.org/10.1016/j.chemgeo.2017.11.006.

Teagle, D.A.H., 1993. A study of hydrothermal alteration of the Troodos ophiolite. Cyprus: Petrological, Geochemical and Strontium Isotopic Constraints. University of Cambridge.

Templeton, A.S., Ellison, E.T., Kelemen, P.B., Leong, J., Boyd, E.S., Colman, D.R., Matter, J.M., 2024. Low-temperature hydrogen production and consumption in partially-hydrated peridotites in Oman: implications for stimulated geological hydrogen production. Front. Geochem. 2, 1366268. https://doi.org/10.3389/fgeoc.2024.1366268.

Thompson, A., Chadwick, O.A., Rancourt, D.G., Chorover, J., 2006. Iron-oxide crystallinity increases during soil redox oscillations. Geochem. Cosmochim. Acta 70, 1710–1727. https://doi.org/10.1016/j.gca.2005.12.005.

Trendall, A.F., Blockey, J.B., 1970. The Iron Formations of the Precambrian Hamersley Group, Western Australia with Special Reference to the Associated Crocidolite. Geological Survey, of Western Australia.

Truche, L., Bourdelle, F., Salvi, S., Lefeuvre, N., Zug, A., Lloret, E., 2021. Hydrogen generation during hydrothermal alteration of peralkaline granite. Geochem. Cosmochim. Acta 308, 42–59. https://doi.org/10.1016/j.gca.2021.05.048.

Tutolo, B.M., Seyfried, W.E., Tosca, N.J., 2020. A seawater throttle on H_2 production in Precambrian serpentinizing systems. Proc. Natl. Acad. Sci. U.S.A 117, 14756–14763. https://doi.org/10.1073/pnas.1921042117.

Van Alboom, A., De Grave, E., 1996. Temperature dependence of the 57Fe Mössbauer parameters in riebeckite. Phys. Chem. Miner. 23, 377–386. https://doi.org/10.1007/BF00199503.

Van Kranendonk, M.J., 2006. Revised Lithostratigraphy of Archean Supracrustal and Intrusive Rocks in the Northern Pilbara Craton. Western Australia. Geological Survey of Western Australia, East Perth, W.A.

Vandenberghe, R.E., De Grave, E., 1989. Mössbauer effect studies of oxidic spinels. In: Long, G.J., Grandjean, F. (Eds.), Mössbauer Spectroscopy Applied to Inorganic Chemistry. Springer US, Boston, MA, pp. 59–182. https://doi.org/10.1007/978-1-4899-2289-2_3.

Wareppam, B., Kuzmann, E., Garg, V.K., Singh, L.H., 2022. Mössbauer spectroscopic investigations on iron oxides and modified nanostructures: a review. J. Mater. Res. https://doi.org/10.1557/s43578-022-00665-4.

Winsett, J., Moilanen, A., Paudel, K., Kamali, S., Ding, K., Cribb, W., Seifu, D., Neupane, S., 2019. Quantitative determination of magnetite and maghemite in iron oxide nanoparticles using Mössbauer spectroscopy. SN Appl. Sci. 1, 1636. https://doi.org/10.1007/s42452-019-1699-2.

Xue, D., Wang, H., Liu, Y., Xie, L., Shen, P., 2017. An improved procedure for the determination of ferrous iron mass fraction in silicate rocks using a schlenk line-based digestion apparatus to exclude oxygen. Geostand. Geoanal. Res. 41, 411–425. https://doi.org/10.1111/ggr.12164.

Yamada, A., Chung, S.C., Hinokuma, K., 2001. Optimized LiFePO[sub 4] for lithium battery cathodes. J. Electrochem. Soc. 148, A224. https://doi.org/10.1149/1.1348257.

Yoshida, Y., Langouche, G. (Eds.), 2013. Mössbauer Spectroscopy: Tutorial Book. Springer Berlin Heidelberg, Berlin, Heidelberg. https://doi.org/10.1007/978-3-642-32220-4.